separations

MDPI

Article

Accessible Surface Area, Not Layer Chemistry, Governs Pb(II) Uptake by Carbonate Layered Double Hydroxides: A Single-Protocol Comparison of $Mg_2Al–CO_3$, $Mg_2[FeAl]–CO_3$ and $Zn_2[FeAl]–CO_3$

Abdeljalil Ait Ichou [1,*], Ridouan Benhiti [1], Mhamed Abali [1], Abdelkader Dabagh [1], Gabriela Carja [2], Amina Soudani [3], Mohamed Chiban [1], Mohamed Zerbet [1] and Fouad Sinan [1]

[1] Laboratory of Applied Chemistry and Environment, Department of Chemistry, Faculty of Sciences, Ibn Zohr University, BP 8106, Cité Dakhla, Agadir 80060, Morocco; b.ridouan@yahoo.fr (R.B.); mhamedabali@gmail.com (M.A.); abdelkader.dabagh@gmail.com (A.D.); mmchiban@yahoo.fr (M.C.); zerbetmohamed@gmail.com (M.Z.); f.sinan@uiz.ac.ma (F.S.)

[2] Department of Chemical Engineering, Faculty of Chemical Engineering and Environmental Protection "Cristofor I. Simionescu", Technical University "Gh. Asachi" of Iasi, Bd. D. Mangeron No. 71, 700554 Iasi, Romania; carja@uaic.ro

[3] Faculty of Applied Sciences Ait Melloul, Ibn Zohr University, Route Nationale N10, BP 6146, Cité Azrou, Ait Melloul 86150, Morocco; a.soudani@uiz.ac.ma

* Correspondence: a.aitichou@uiz.ac.ma

Abstract

The removal of Pb(II) ions from aqueous solution by sorption onto layered double hydroxides (LDHs) is widely documented, yet the reported capacities range from about 60 to about 120 mg g^{-1}. This dispersion is usually ascribed to the layer chemistry, but this attribution cannot be tested because the published values were obtained under widely different operating conditions; this work supplies the missing reference member of a single-protocol series. Carbonate-intercalated $Mg_2Al–CO_3$ was prepared by coprecipitation at constant pH, characterized by XRD, SEM–EDX, N_2 sorption, DSC and pH_{PZC} measurement, and evaluated as a function of sorbent dose, pH, contact time, initial concentration and temperature. Equilibrium was reached within 60 min; the kinetics followed the pseudo-first-order model; the Redlich–Peterson and Langmuir equations best fitted the isotherm (monolayer capacity, 59.1 mg g^{-1}); and the uptake was spontaneous and endothermic (ΔH° = 11.1 kJ mol^{-1}). These results were then compared with those previously published by our group for two isostructural phases, $Mg_2[FeAl]–CO_3$ and $Zn_2[FeAl]–CO_3$, prepared and tested under strictly identical conditions; no new experiments were performed on these solids, whose values are quoted for comparison only. Replacing half of the Al(III) with Fe(III) doubled q_m to 118.8 mg g^{-1}, whereas further replacing Mg(II) with Zn(II) lowered it to 87.9 mg g^{-1}. Normalized to the BET surface area, however, the three capacities converge on 1.55 ± 0.07 mg m^{-2}: the layer composition acts on Pb(II) uptake only through the accessible surface area it generates, not through the intrinsic reactivity of the surface. Sorbent design should therefore target textural disorder rather than a particular cation pair.

Keywords: layered double hydroxide; $Mg_2Al–CO_3$; lead removal; sorption isotherms; crystallinity; cationic substitution; water treatment

Check for updates

Academic Editors: Jelena Mitrović, Nena Velinov and Miljana Radović Vučić

Received: 5 September 2026
Revised: 27 September 2026
Accepted: 29 September 2026
Published: 1 October 2026

Copyright: © 2026 by the authors. Licensee MDPI, Basel, Switzerland. This article is an open access article distributed under the terms and conditions of the Creative Commons Attribution (CC BY) license.

1. Introduction

Contamination of aquatic systems by potentially toxic metals remains one of the most persistent environmental problems associated with mining, metal finishing, battery manufacturing, pigment production and the uncontrolled reuse of urban wastewater in irrigation [1,2]. Unlike most organic pollutants, these elements are neither biodegradable nor destroyed by thermal treatment; they accumulate along the food chain and remain bioavailable for very long periods [3]. Lead is particularly problematic: it has no known physiological function, it interferes with heme biosynthesis and with neuronal development, and the World Health Organization recommends a provisional guideline value of only 10 μg L^{-1} in drinking water [4]. Industrial effluents, however, routinely contain lead at concentrations of tens to hundreds of mg L^{-1}, so an efficient treatment step is required before discharge.

Several technologies have been proposed for this purpose, including chemical precipitation, membrane filtration, electrodialysis, solvent extraction and ion exchange [5,6]. Most of them suffer from high operating costs, high sludge production or poor efficiency in the low-concentration range. Sorption remains the most attractive option for small and medium-sized facilities because it is simple to operate, tolerant of fluctuations in the feed and compatible with a wide range of inexpensive materials, from agricultural residues and plant biomass [7–10] to engineered inorganic solids [11].

Among the latter, layered double hydroxides (LDHs), also known as anionic clays or hydrotalcite-like compounds, have attracted sustained attention. Their structure derives from brucite, $Mg(OH)_2$: some of the divalent cations of the octahedral sheet are replaced isomorphically by trivalent cations, which generates a positive layer charge balanced by hydrated interlayer anions. The resulting composition is described by the general formula $[M^{II}_{1-x}M^{III}_{x}(OH)_2]^{x+}[A^{n-}]_{x/n}\cdot yH_2O$, with $x = M^{III}/(M^{II} + M^{III})$ usually restricted to 0.20–0.40 [12–14]. LDHs are inexpensive, non-toxic, thermally robust and, above all, chemically tunable: the nature of metal cations, their ratio and the interlayer anion can be selected almost independently, which explains their use in catalysis, drug delivery, flame retardancy and water decontamination [9,15–20].

The removal of anionic pollutants by LDHs, which proceeds essentially through anion exchange and the so-called memory effect, is now well understood [15,21–24]. The uptake of metal cations is a more subtle question, because the sorbate carries a charge of the same sign as the layers. Nonetheless, LDHs remove Cu(II), Pb(II) and Cd(II) efficiently through a combination of surface complexation, surface precipitation, isomorphic substitution and, when chelating anions are intercalated, interlayer complexation [25–32]. Reported capacities span more than one order of magnitude [25,33–35], from about 19 mg g^{-1} for glutamate-intercalated Mg_2Al–LDH [36] to more than 500 mg g^{-1} for MOF-derived phases [37].

This dispersion is usually attributed to the chemistry of the sorbent, yet this attribution is very difficult to verify, because the published results were obtained at different initial concentrations, solid-to-liquid ratios, contact times and pH values. Comparisons carried out under strictly identical conditions remain rare [38]; the few available examples, such as the study of Zn–Al and Mg–Al LDHs for perfluorooctanoic acid [39] or the comparison of MgAl-LDHs obtained through different synthesis routes [40,41], show that apparently minor changes in composition or crystallinity can alter the capacity by a factor of two or more. Moreover, the simplest and cheapest member of the family, the binary Mg_2Al–CO_3 phase, is frequently used as an implicit reference without having been characterized and evaluated under the same protocol as the substituted phases with which it is compared.

The present work addresses this gap. A carbonate-intercalated Mg_2Al–CO_3 phase was synthesized by coprecipitation at constant pH, fully characterized, and evaluated

for Pb(II) removal from aqueous solution. The effects of sorbent dose, initial pH, contact time, initial metal concentration and temperature were quantified, and kinetic, equilibrium, thermodynamic and energetic models were applied in their non-linear forms. The results are then compared with those we previously published for two isostructural ternary phases, Mg_2[FeAl]–CO_3 [42] and Zn_2[FeAl]–CO_3 [43], prepared and tested in the same laboratory under strictly identical operating conditions. This comparison is the main purpose of the study rather than a complement to it: because the three solids share the same synthesis route, interlayer anion, nominal M^{II}/M^{III} ratio (2) and test protocol, the differences between them can be attributed to the composition of the hydroxide layer alone, which is impossible with literature data obtained under different conditions. Moreover, the three phases form a stepwise series in which each step changes a single cation—partial substitution of Al^{III} by Fe^{III} in the trivalent position (Mg_2Al–CO_3 → Mg_2[FeAl]–CO_3), then replacement of Mg^{II} by Zn^{II} in the divalent position (Mg_2[FeAl]–CO_3 → Zn_2[FeAl]–CO_3). The comparison therefore isolates two design variables that are normally confounded and relates them quantitatively to crystallinity, specific surface area and Pb(II) uptake.

2. Materials and Methods

2.1. Reagents

Magnesium chloride hexahydrate ($MgCl_2 \cdot 6H_2O$), aluminum chloride hexahydrate ($AlCl_3 \cdot 6H_2O$), sodium hydroxide, sodium carbonate and lead(II) nitrate ($Pb(NO_3)_2$), supplied by Fluka (Buchs, Switzerland), and silver nitrate ($AgNO_3$), sodium perchlorate ($NaClO_4$), hydrochloric acid, methanol, formaldehyde and the pH buffer standards, supplied by Sigma-Aldrich (Merck, Darmstadt, Germany), were of analytical grade and used without further purification. All solutions were prepared with bi-distilled water. A 1 g L^{-1} Pb(II) stock solution was prepared from $Pb(NO_3)_2$ and diluted as required; the pH of the working solutions was not adjusted unless explicitly stated.

2.2. Synthesis of the LDH Phases

Mg_2Al–CO_3 was obtained by coprecipitation at low supersaturation and constant pH [12,14]. A salt solution containing $MgCl_2 \cdot 6H_2O$ and $AlCl_3 \cdot 6H_2O$ in a Mg^{II}/Al^{III} molar ratio of 2 was added dropwise, together with an alkaline solution of NaOH and Na_2CO_3 (CO_3^{2-}/Al^{III} = 2), to 500 mL of vigorously stirred deionized water. The pH was held at 10.0 ± 0.05 by the controlled addition of 2 M NaOH. The resulting suspension was subjected to hydrothermal aging at 80 °C for 24 h under mechanical stirring, recovered by filtration and washed repeatedly with deionized water. After each washing cycle, the filtrate was tested for chloride with a few drops of $AgNO_3$ solution (0.1 M), and washing was continued until no white AgCl precipitate or turbidity was observed. The solid was then dried under vacuum at 80 °C for 10 h, ground and sieved to below 149 µm. The absence of residual chloride and sodium in the final solid was confirmed by EDX analysis (Section 3.1.2).

2.3. Characterization

Powder X-ray diffraction (XRD) patterns were collected in air on a PANalytical X'Pert Pro diffractometer (Malvern Panalytical, Almelo, The Netherlands) using monochromatized Cu Kα_1 radiation (λ = 1.54060 Å) at 45 kV and 40 mA, over the 3–80° 2θ range with a step of 0.067°. Phase identification was carried out with Match! software, version 3.7.1.132 (Crystal Impact, Bonn, Germany), against the ICDD PDF-2 database, release 2018 (International Centre for Diffraction Data, Newtown Square, PA, USA). The lattice parameters of the rhombohedral cell (space group $R\bar{3}m$) were derived from the positions of the (003) and (110) reflections, $c = 3d_{003}$ and $a = 2d_{110}$. The relative crystallinity was estimated from the

integrated intensity of the basal reflections using the peak-analyzer routine of OriginPro 9.1 (OriginLab Corporation, Northampton, MA, USA), the most intense pattern available in our LDH series being taken as the reference, so that the values reported here and in our previous studies are directly comparable [42,43].

Morphology and surface composition were examined with a TESCAN VEGA3 scanning electron microscope (Brno, Czech Republic) equipped with an energy-dispersive X-ray (EDX) detector operated at 25 kV. Nitrogen adsorption–desorption isotherms were recorded at 77 K on an ASAP 2010 instrument (Micromeritics, Norcross, GA, USA) after outgassing. Specific surface areas were computed by the BET method in the $0.05 < P/P^\circ < 0.30$ range [44], micropore areas by the t-plot method, and pore size distributions by the BJH method applied to the desorption branch [45]; isotherms were classified according to the IUPAC recommendations [46]. Thermal behavior was followed by differential scanning calorimetry (DSC, TA Instruments Q100, TA Instruments, New Castle, DE, USA) between 40 and 500 °C at 10 °C min^{-1} under a 50 mL min^{-1} nitrogen flow. The point of zero charge (pH_{PZC}) was determined by the batch equilibration method [47,48], the pH_{PZC} being read at the intersection of the $pH_f = f(pH_i)$ curve with the first bisector.

2.4. Batch Sorption Experiments

Sorption experiments were carried out in batch mode. A known mass of LDH was contacted with 20 mL of Pb(II) solution in stoppered flasks immersed in a thermostated bath and stirred magnetically to avoid settling. After the required contact time, the suspensions were centrifuged at 500 rpm, and the final pH (pH_f) was measured with a Consort SP20T pH meter calibrated with pH 4, 7 and 10 buffer standards. Residual Pb(II) was determined with a Consort C863 ionometer fitted with an SE30B lead-selective electrode (both from Consort, Turnhout, Belgium); 50 mL of sample was mixed with 50 mL of a methanol/formaldehyde medium and 2 mL of 5 M $NaClO_4$ as the ionic-strength adjuster. The 50 mL sample was obtained by a five-fold dilution of the supernatant (10 mL diluted to 50 mL). All experiments were run in triplicate, and the results are reported as mean values; the values of each replicate, with their standard deviation (SD) and relative standard deviation (RSD), are given in Section S8 of the Supplementary Materials (Tables S8–S15). The RSD did not exceed 3%.

The effect of the sorbent dose was evaluated by contacting increasing masses of $Mg_2Al–CO_3$ (10–100 mg) with 20 mL of a 100 mg L^{-1} Pb(II) solution, i.e., solid-to-liquid ratios m/V of 0.5, 1.0, 1.5, 1.75, 2.0, 2.5, 3.0, 3.5, 4.0 and 5.0 g L^{-1}, at the natural pH of the solution (pH_i = 5.45), for 3 h at 25 °C. After centrifugation, the residual Pb(II) concentration and the final pH were measured as described above, and the removal efficiency and the amount sorbed were calculated with Equations (1) and (2). The ratio giving the highest amount sorbed per unit mass, 1.75 g L^{-1}, was retained for all subsequent experiments; this ratio was also used for the two comparison phases (Section 2.6). The effect of the initial pH was then studied between 2 and 10 (adjusted with 1 M HCl or 1 M NaOH); the kinetics between 5 and 180 min; the effect of the initial concentration between 10 and 300 mg L^{-1}; and the effect of temperature between 15 and 60 °C. Unless otherwise specified, the operating conditions were C_0 = 100 mg L^{-1}, m/V = 1.75 g L^{-1}, t_c = 3 h, T = 25 °C and pH_i = 5.45 (unadjusted).

The removal efficiency R (%) and the amount sorbed at equilibrium q_e (mg g^{-1}) were computed as

$$R(\%) = \frac{(C_0 - C_t)}{C_0} \times 100 \quad (1)$$

and

$$q_e = (C_0 - C_e)\frac{V}{m} \quad (2)$$

where C_0, C_t and C_e (mg L^{-1}) are the initial, instantaneous and equilibrium Pb(II) concentrations, V (L) the solution volume and m (g) the sorbent mass.

2.5. Modeling

Kinetic data were analyzed with the pseudo-first-order (PFO) [49], pseudo-second-order (PSO) [50], Elovich and intraparticle diffusion (IPD) [51] models, written in their non-linear forms:

$$q_t = q_e(1 - e^{-k_1 t}) \quad (3)$$

$$q_t = k_2\, q_e^2\, t/(1 + k_2\, q_e\, t) \quad (4)$$

$$q_t = \frac{1}{\beta} \ln(\alpha\beta) + \frac{1}{\beta} \ln(t) \quad (5)$$

$$q_t = K_{IPD} t^{1/2} + C \quad (6)$$

where k_1 (min^{-1}), k_2 (g mg^{-1} min^{-1}) and k_{IPD} (mg g^{-1} $min^{-1/2}$) are the corresponding rate constants, α (mg g^{-1} min^{-1}) is the initial sorption rate, β (g mg^{-1}) the desorption constant and C (mg g^{-1}) a constant proportional to the boundary-layer thickness. Equilibrium data were described by the Langmuir [52], Freundlich [53], Redlich–Peterson [54] and Temkin [55] isotherms:

$$q_e = q_m K_L C_e/(1 + K_L C_e) \quad (7)$$

$$R_L = 1/(1 + K_L C_0) \quad (8)$$

$$q_e = K_F C_e^{1/n} \quad (9)$$

$$q_e = K_{R-P} C_e/(1 + \alpha_{R-P} C_e{}^{*\beta *}) \quad (10)$$

$$q_e = (RT/b_T) \ln(A_T C_e) \quad (11)$$

where q_m (mg g^{-1}) is the monolayer capacity and K_L (L mg^{-1}) the Langmuir constant; R_L is the dimensionless separation factor; K_F ($mg^{1-1/n}$ $L^{1/n}$ g^{-1}) is the Freundlich constant and $1/n$ the heterogeneity factor; K_{R-P} (L g^{-1}), α_{R-P} ((L $mg^{-1})^{\beta}$) and β ($0 < \beta \leq 1$) are the Redlich–Peterson constants; and $B = RT/b_T$ (mg g^{-1}) and A_T (L mg^{-1}) are the Temkin constants related to the heat of sorption and to the equilibrium binding energy, respectively.

The enthalpy of sorption was obtained from the temperature dependence of the distribution coefficient $K_d = q_e/C_e$ through the van 't Hoff relationship, whose slope is not affected by the constant factor used to render the equilibrium constant dimensionless; the Gibbs energy and the entropy were referred to the IUPAC standard concentration C° = 1 mol L^{-1} through $K^\circ = K_L$(L mol^{-1})/C°, as recommended for solid–liquid adsorption systems [56]:

$$\Delta G^\circ = -RT \ln K_c \quad (12)$$

$$\ln K_c = (\Delta S^\circ/R) - (\Delta H^\circ/RT) \quad (13)$$

so that

$$\Delta G^\circ = \Delta H^\circ - T\Delta S^\circ \quad (14)$$

The mean free energy of sorption was estimated from the Dubinin–Radushkevich (D–R) isotherm [57]:

$$q_e = q_{m,D-R} \exp(-K_{D-R}\varepsilon^2),\ \varepsilon = RT \ln(1 + 1/C_e) \quad (15)$$

$$E_{D-R} = 1/(2K_{D-R})^{1/2} \quad (16)$$

All models were fitted by non-linear regression (orthogonal distance regression) with OriginPro 9.1. The goodness of fit was assessed jointly from the coefficient of determination (R^2) and the chi-square statistic (χ^2).

$$\chi^2 = \Sigma\,(q_{e,exp} - q_{e,cal})^2/(N - p) \quad (17)$$

where N is the number of experimental points and p the number of adjustable parameters (reduced chi-square).

Non-linear fitting was preferred to the linearized forms because the latter distort the error structure and may lead to inconsistent parameter estimates [56].

2.6. Reference Materials Used for Comparison

Two ternary carbonate phases previously prepared and evaluated in our laboratory are used in Section 4 as comparison materials: Mg_2[FeAl]–CO_3, in which half of the trivalent position is occupied by Fe^{III} [42], and Zn_2[FeAl]–CO_3, in which the divalent position is occupied by Zn^{II} [43]. Both were obtained by the same coprecipitation protocol at constant pH followed by hydrothermal aging at 80 °C for 24 h, characterized with the same instruments, and tested with the same batch procedure, the same lead-selective electrode method and the same reference conditions (C_0 = 100 mg L^{-1}, m/V = 1.75 g L^{-1}, t_c = 3 h, T = 25 °C, unadjusted pH). No new experiment was performed on these two solids in the present study; all values quoted for them are taken from the corresponding publications and are cited as such throughout.

3. Results

3.1. Characterization of Mg_2Al–CO_3

3.1.1. X-Ray Diffraction

The diffraction pattern of the synthesized solid is shown in Figure 1 together with the line positions and relative intensities of the reference card PDF-2 01-089-0460, $Mg_{0.667}Al_{0.333}(OH)_2(CO_3)_{0.167}\cdot 0.5H_2O$, for which a figure of merit of 0.892 was obtained; the complete list of interplanar distances is given in Table S1. The pattern displays the sharp, symmetric basal reflections and the resolved (110)/(113) doublet above 60° 2θ that are characteristic of a well-crystallized hydrotalcite-like phase, and it can be divided into the three domains usually distinguished for LDHs: the (00l) reflections below 30° 2θ, whose position is governed by the size of the interlayer anion, the (01l) reflections between 30 and 50°, and the (11l) reflections above 50°, which reflect the cation order within the hydroxide sheets. All the observed reflections were indexed in a trigonal system with rhombohedral symmetry ($R\bar{3}m$). The strongest reflection, (003), lies at 11.61° 2θ and corresponds to a basal spacing d_{003} = 7.61 Å. The derived lattice parameters are c = 22.84 Å and a = 3.0434 Å, and the relative crystallinity is 68.0% (Table 1). The agreement with the reference card is close for every line except in the 34–35° region: the measured maximum at 34.88° is the (012) reflection, whereas the strongest card line in that range, at 34.19°, is the (101) reflection. The two are not resolved in the present pattern and merge into a single asymmetric envelope whose low-angle shoulder is the (101) contribution, a feature commonly observed for hydrotalcite-like phases whose sheet stacking is not perfectly ordered.

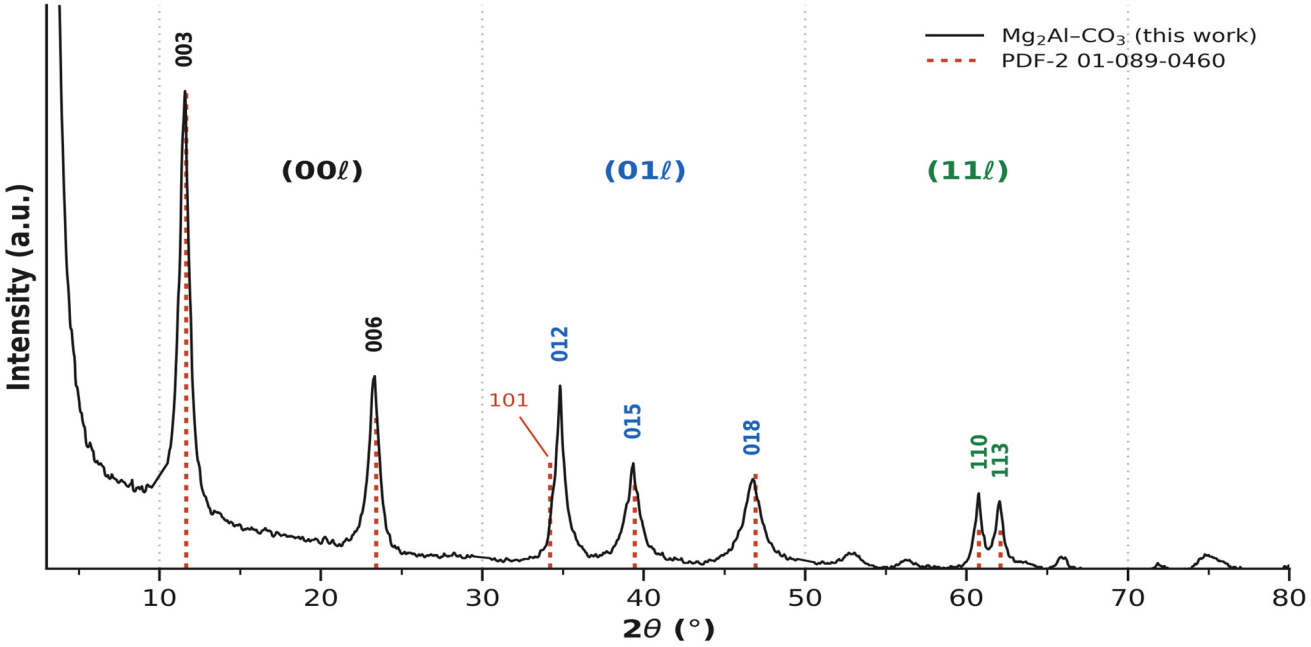


Figure 1. XRD pattern of $Mg_2Al–CO_3$ (Cu Kα_1, 3–80° 2θ) with the reference card PDF-2 01-089-0460 shown as dotted lines.

Table 1. Structural, compositional, textural and surface properties of the $Mg_2Al–CO_3$ phase prepared in this work.

Property	Value	Technique/Remark
a (Å)	3.0434	XRD, $a = 2d_{110}$
c (Å)	22.8402	XRD, $c = 3d_{003}$
d_{003} (Å)	7.61	XRD, basal spacing
Relative crystallinity (%)	67.96	XRD, integrated basal intensities
Mg/Al ratio	1.69	EDX (nominal value 2)
$x = Al^{III}/(Mg^{II} + Al^{III})$	0.372	EDX
Proposed formula	$Mg_{0.63}Al_{0.37}(OH)_2(CO_3)_{0.18}\cdot yH_2O$	
S_{BET} ($m^2\ g^{-1}$)	37.83	N_2 sorption, 77 K
Micropore area (%)	19.47	t-plot method
Mean pore diameter (nm)	6.62	BJH, desorption branch
Total pore volume ($cm^3\ g^{-1}$)	0.05188	at $P/P^\circ = 0.8962$
Equivalent particle size (nm)	158.59	from S_{BET}
DSC endotherms (°C)	125, 225, >275	10 °C min^{-1}, N_2
pH_{PZC}	9.25	batch equilibration

3.1.2. Morphology and Surface Composition

The morphology of the powder was examined by scanning electron microscopy at three magnifications (Figure S1). The solid consists of strongly agglomerated micrometric particles of irregular shape and heterogeneous size, with no individual platelet being resolved even at 5.00 kx; this compact aspect is consistent with the modest specific surface area reported below and with the equivalent particle size of 158.6 nm derived from it. EDX analysis of the surface (Figure S2 and Table S2) detects carbon, magnesium, aluminum and oxygen as the only elements and gives 21.4 at.% Mg and 12.7 at.% Al, that is, an experimental Mg/Al ratio of 1.69 against a nominal value of 2; neither chlorine nor sodium was detected, which confirms the efficiency of the washing procedure (Section 2.2). Combining the EDX composition with the general LDH formula yields the approximate composition $Mg_{0.63}Al_{0.37}(OH)_2(CO_3)_{0.18}\cdot yH_2O$, i.e., a layer charge density $x = 0.372$. Because EDX is a

semi-quantitative, surface-sensitive technique that does not detect hydrogen and quantifies light elements only approximately, this formula is given as indicative: establishing it independently would require ICP-OES for the cations, elemental analysis for the carbonate and thermogravimetry for y, and none of the conclusions drawn below rests on it.

3.1.3. Textural Properties

The nitrogen adsorption–desorption isotherm is of type IV with a narrow hysteresis loop. The BET surface area is 37.8 $m^2\ g^{-1}$, of which 19.5% is contributed by micropores and 80.5% by the external surface. The mean BJH pore diameter is 6.6 nm, the total pore volume 0.0519 $cm^3\ g^{-1}$ and the equivalent particle size 158.6 nm (Table S3).

3.1.4. Thermal Behavior

The DSC curve (Figure S3) exhibits three successive endothermic events: a broad signal extending from room temperature to about 200 °C with a minimum near 125 °C, assigned to the loss of physisorbed water; a second, narrower event between 200 and 250 °C with a minimum at 225 °C, assigned to the loss of interlayer water, which proceeds without collapse of the layered structure; and a third, beginning above 275 °C and continuing to the end of the scan, which combines the dehydroxylation of the brucite-like sheets and the decarbonation of the interlayer. The first two events are reversible and underlie the rehydration behavior of carbonate LDHs, whereas the third destroys the layered structure and yields the mixed oxide.

3.1.5. Point of Zero Charge

The $pH_f = f(pH_i)$ curve (Figure S4) shows a plateau between pH_i 8 and 10, which defines the buffering domain of the solid, and intersects the first bisector at pH 9.25, which is the point of zero charge of the material. All the characterization results are collected in Table 1. It should be stressed at this stage that every sorption experiment carried out at the natural pH of the solution (i.e., all the experiments except those of Section 3.2.2) ended at a final pH between 5.5 and 6.3, that is, well below pH_{PZC}, so that the surface carried a net positive charge throughout; this constraint governs the discussion of the removal mechanism in Section 4.

3.2. Pb(II) Sorption on Mg_2Al–CO_3

3.2.1. Effect of the Sorbent Dose

Increasing the m/V ratio from 0.5 to 5 g L^{-1} raises the removal efficiency of Pb(II) monotonically from 13.1 to 84.3% (Figure 2a), because the number of available sorption sites increases with the mass of solid. The capacity per unit mass follows a different trend (Figure 2b): it remains almost constant between 0.5 and 1.5 g L^{-1} (26.2–26.6 mg g^{-1}), passes through a maximum of 27.11 mg g^{-1} at 1.75 g L^{-1}, and then decreases steadily to 16.86 mg g^{-1} at 5 g L^{-1}. Beyond 1.75 g L^{-1}, the amount of lead available is no longer sufficient to saturate the sites provided by the additional solid, so that some of them remain unoccupied and the amount sorbed per unit mass decreases. The final pH rose only moderately over the same interval, from 5.54 to 6.30. The complete data set is reported in Table S4. The ratio of 1.75 g L^{-1}, which gives the highest capacity per unit mass, was retained for all subsequent experiments; it is also the ratio used for Mg_2[FeAl]–CO_3 and Zn_2[FeAl]–CO_3 [42,43], so that the three solids are compared under identical conditions.

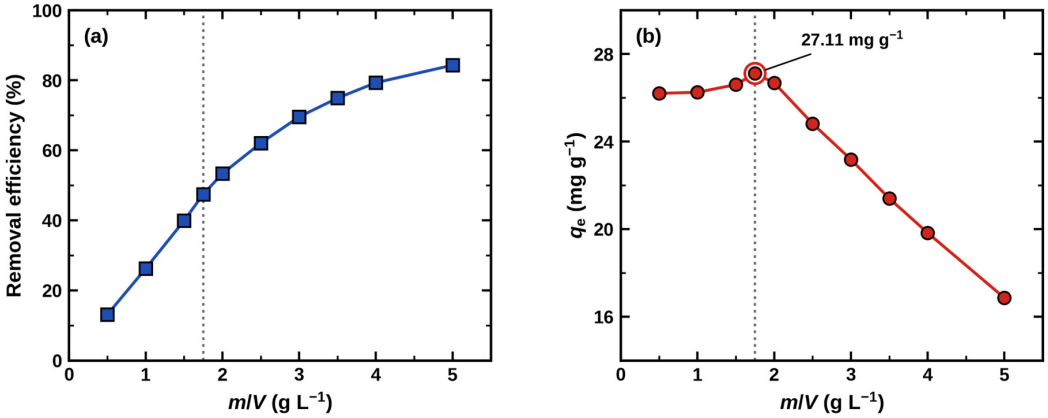


Figure 2. Effect of the sorbent dose on Pb(II) sorption by $Mg_2Al–CO_3$: (**a**) removal efficiency; (**b**) equilibrium capacity. The dotted line marks the ratio m/V = 1.75 g L^{-1} retained for the rest of the study (C_0 = 100 mg L^{-1}, V = 20 mL, pH_i = 5.45, t_c = 3 h, T = 25 °C). The values of the three replicates are given in Tables S8 and S9.

3.2.2. Effect of the Initial pH

The uptake of Pb(II) is strongly pH-dependent (Figure S5). At pH_i = 2 the capacity is only about 6 mg g^{-1}. It rises slowly up to pH_i = 4, then sharply between pH_i 4 and 8, and reaches 57.14 mg g^{-1} at $pH_i \approx 8$, a value that corresponds to the quantitative removal of the lead initially present. Beyond pH_i = 8 the capacity can no longer increase, since all the lead has already been removed from the solution. The experiments that ended at a final pH above 7.5, where the precipitation of $Pb(OH)_2$ may contribute to the removal (Section 4.1), are identified in Figure S5 and must be interpreted with caution. In all the experiments carried out at the unadjusted pH (pH_i = 5.45; Sections 3.2.1 and 3.2.3–3.2.5), the final pH remained between 5.5 and 6.3.

3.2.3. Sorption Kinetics

The uptake curve rises steeply during the first 30 min, during which about 85% of the total quantity is retained, then more slowly between 30 and 60 min, and finally levels off (Figure 3). No further variation was measured between 60 and 180 min, so equilibrium is reached within one hour, with $q_{e,exp}$ = 27.15 mg g^{-1}.

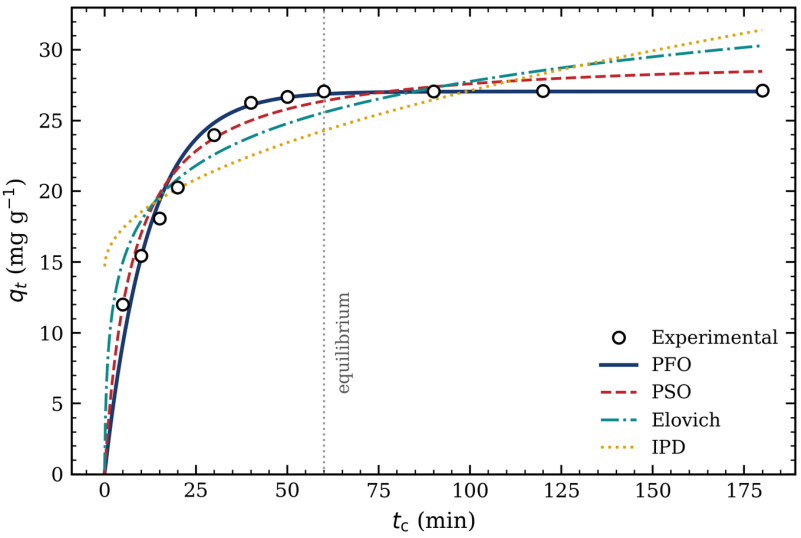


Figure 3. Non-linear modeling of the sorption kinetics of Pb(II) on $Mg_2Al–CO_3$ with the PFO, PSO, Elovich and IPD equations (C_0 = 100 mg L^{-1}, m/V = 1.75 g L^{-1}, pH_i = 5.45, T = 25 °C). Symbols: experimental data; lines: fitted models. The values of the three replicates are given in Table S10.

The parameters obtained for the four models are collected in Table 2. The PFO equation gives the highest determination coefficient (R^2 = 0.99991) and the lowest chi-square (χ^2 = 0.416), and its calculated capacity, 27.054 mg g^{-1}, differs from the experimental value by less than 0.1 mg g^{-1}. The PSO equation also reproduces the data closely (R^2 = 0.99976) but overestimates q_e by 2.5 mg g^{-1} and gives a chi-square nearly three times larger. The Elovich and IPD equations give the largest deviations, with χ^2 of 5.43 and 14.66, respectively. Plotted in its linearized form, $q_t = f(t_c^{1/2})$, the IPD model yields three successive straight segments rather than a single line, none of which passes through the origin (Figure S6 and Table S5).

Table 2. Non-linear kinetic parameters for Pb(II) sorption on Mg_2Al–CO_3 (C_0 = 100 mg L^{-1}, m/V = 1.75 g L^{-1}, pH_i = 5.45, T = 25 °C).

Model	Parameter	Value	R^2	χ^2
Experimental	$q_{e,exp}$ (mg g^{-1})	27.15	—	—
PFO	$q_{e,cal}$ (mg g^{-1})	27.054	0.99991	0.416
	k_1 (min^{-1})	0.08340		
PSO	$q_{e,cal}$ (mg g^{-1})	29.659	0.99976	1.109
	k_2 (g mg^{-1} min^{-1})	0.00452		
Elovich	α (mg g^{-1} min^{-1})	27.115	0.99881	5.430
	β (g mg^{-1})	0.2322		
IPD	k_{IPD} (mg g^{-1} $min^{-1/2}$)	1.2555	0.99679	14.664
	C (mg g^{-1})	14.561		

3.2.4. Effect of the Initial Concentration and Equilibrium Isotherms

The equilibrium capacity increases with the initial concentration over the whole range investigated, from 4.26 mg g^{-1} at 10 mg L^{-1} to 46.31 mg g^{-1} at 300 mg L^{-1} (Figure S7 and Table S6). The increase is almost linear up to 200 mg L^{-1} and becomes much slower beyond, the last three points (44.14, 45.09 and 46.31 mg g^{-1}) marking the onset of a plateau. The highest capacity measured directly is therefore 46.31 mg g^{-1}; the monolayer capacity extracted from the Langmuir fit is given below and is the value used throughout the discussion. The final pH decreased slightly and regularly as the initial concentration increased, from 6.23 to 5.76.

The four isotherm equations were fitted to the experimental points (Figure 4) and the resulting parameters are listed in Table 3. The Redlich–Peterson and Langmuir models give the highest determination coefficients (0.98928 and 0.98921) and the lowest chi-square values (3.909 and 3.373); the Redlich–Peterson exponent β is 0.963, close to unity, so that the equation tends toward the Langmuir limit. The Langmuir monolayer capacity is 59.1 mg g^{-1} and the separation factor R_L, computed from Equation (8), decreases regularly from 0.84 at C_0 = 10 mg L^{-1} to 0.15 at C_0 = 300 mg L^{-1}, so that $0 < R_L < 1$ over the whole concentration range, which indicates favorable sorption. In the Freundlich equation (Equation (9)), the fitted heterogeneity factor is $1/n = 0.455$, i.e., $n = 2.20$; a value of n greater than unity ($0 < 1/n < 1$) again indicates a favorable isotherm. The Temkin equation gives the lowest R^2 (0.95111) and the highest χ^2 (15.279).

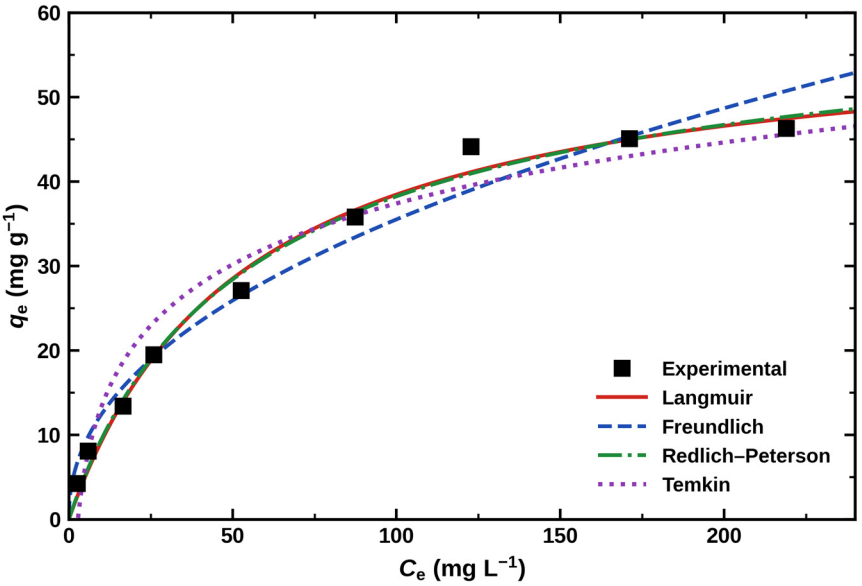


Figure 4. Non-linear modeling of the Pb(II) sorption isotherm on Mg_2Al–CO_3 with the Langmuir, Freundlich, Redlich–Peterson and Temkin equations (m/V = 1.75 g L^{-1}, t_c = 3 h, T = 25 °C). Symbols: experimental data; lines: fitted models. The values of the three replicates are given in Table S11.

Table 3. Non-linear isotherm parameters for Pb(II) sorption on Mg_2Al–CO_3 (m/V = 1.75 g L^{-1}, t_c = 3 h, T = 25 °C).

Model	Parameters	Value	R^2	χ^2
Langmuir	q_m (mg g^{-1})	59.06	0.98921	3.373
	K_L (L mg^{-1})	0.01867		
	R_L	0.152		
Freundlich	K_F (mg$^{1-1/n}$ L$^{1/n}$ g^{-1})	4.374	0.96963	9.494
	$1/n$	0.45478 (n = 2.199)		
Redlich–Peterson	$K_{R–P}$ (L g^{-1})	1.16459	0.98928	3.909
	$\alpha_{R–P}$ (L mg^{-1})$^{\beta}$	0.02426		
	β	0.96290		
Temkin	$B = RT/b_T$ (mg g^{-1})	10.427	0.95111	15.279
	A_T (L mg^{-1})	0.36142		
Dubinin–Radushkevich	$q_{m,D–R}$ (mg g^{-1})	56.40	0.97331	8.343
	$K_{D–R}$ (mol^2 kJ^{-2})	0.25250		
	$E_{D–R}$ (kJ mol^{-1})	1.407		

R_L computed from Equation (8) at C_0 = 300 mg L^{-1}.

3.2.5. Effect of Temperature

Raising the temperature from 15 to 60 °C increases the amount of Pb(II) retained from 25.20 to 34.06 mg g^{-1}, that is, from 44.1 to 59.6% removal (Figure 5a and Table S12); the increase is regular over the whole range, which indicates that the process is endothermic. The van 't Hoff plot of ln K_c against $1/T$ is linear (R^2 = 0.9977, Figure 5b), and its slope gives ΔH° = 11.07 kJ mol^{-1}. This enthalpy does not depend on the standard state adopted, since a constant multiplicative factor applied to the equilibrium constant shifts the intercept of the van 't Hoff line but not its slope. The Gibbs energy and the entropy, in contrast, do depend on that choice and were therefore evaluated from the Langmuir constant expressed in L mol^{-1} and referred to the IUPAC standard concentration C° = 1 mol L^{-1}: with K_L = 0.01867 L mg^{-1}, that is 3.87 × 10^3 L mol^{-1}, one obtains K° = 3.87 × 10^3, ΔG°(298 K) = −20.5 kJ mol^{-1} and, through $\Delta S^\circ = (\Delta H^\circ - \Delta G^\circ)/T$, ΔS° = 106 J mol^{-1} K^{-1} (Table 4). The negative ΔG° confirms that the uptake is spontaneous, and the positive ΔS° reflects the increase in disorder at the solid–solution interface

that accompanies the release of hydration water when the metal ion binds to the surface. Because the isotherm was recorded at a single temperature, the standard Gibbs energy referred to C° = 1 mol L^{-1} could only be determined at 298 K; the ΔG values listed in Table 4 for each temperature, including 298 K, are apparent values calculated from K_c ($\Delta G_{app} = -RT \ln K_c$), which are not referred to the standard state but show the same trend, the uptake becoming more favorable as the temperature increases.

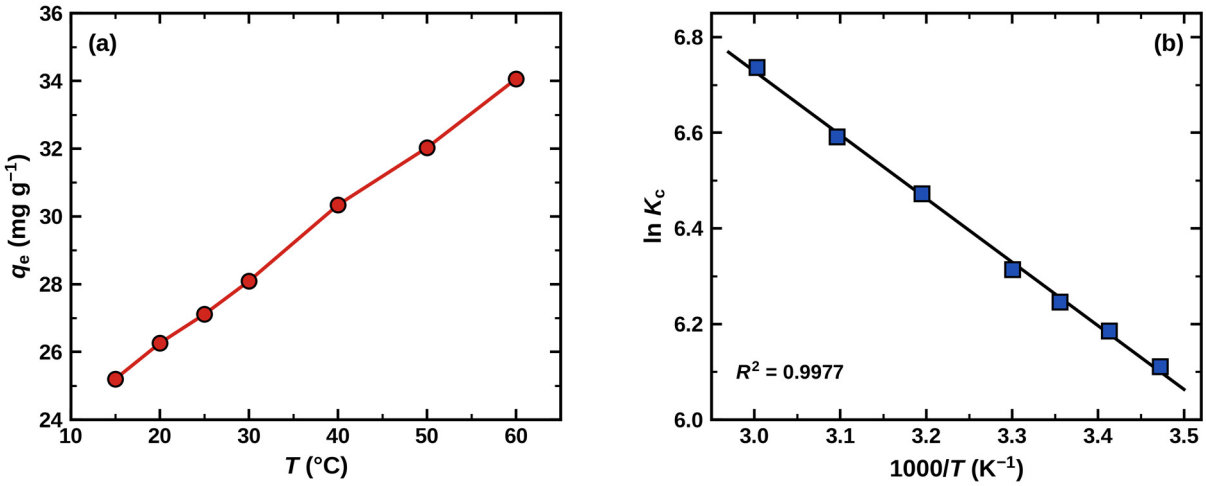


Figure 5. (**a**) Effect of temperature on the equilibrium capacity of Mg_2Al–CO_3 toward Pb(II); (**b**) corresponding van 't Hoff plot (C_0 = 100 mg L^{-1}, m/V = 1.75 g L^{-1}, t_c = 3 h, pH_i = 5.45). The values of the three replicates of panel (**a**) are given in Table S12.

Table 4. Thermodynamic and energetic parameters for Pb(II) sorption on Mg_2Al–CO_3 (C_0 = 100 mg L^{-1}, m/V = 1.75 g L^{-1}, t_c = 3 h).

T (K)	K_c [a]	ΔG_{app} (kJ mol^{-1}) [b]	ΔH° (kJ mol^{-1})	ΔS° (J mol^{-1} K^{-1})
288	450.81	−14.640		
293	485.79	−15.076		
298	515.97	−15.483		
303	552.32	−15.914	11.072	105.8
313	646.97	−16.851		
323	728.75	−17.709		
333	843.00	−18.660		
Energetic parameters			E_{D-R} = 1.407 kJ mol^{-1}	ΔG°(298 K) = −20.5 kJ mol^{-1}

[a] K_c = 1000 q_e/C_e (L kg^{-1}), used for the van 't Hoff plot (Figure 5b). [b] Apparent Gibbs energy, $\Delta G_{app} = -RT \ln K_c$, not referred to the standard state; the standard values ΔG°(298 K) and ΔS° are referred to C° = 1 mol L^{-1} (Section 2.5).

4. Discussion

4.1. Surface Charge and Lead Speciation

The pH dependence reported in Section 3.2.2 (Figure S5) combines two effects. At low pH the surface is protonated, and the large excess of H^+ competes with Pb^{2+} for the binding sites; partial dissolution of the hydroxide layers may also occur in strongly acidic media. As the pH increases toward the point of zero charge measured here, 9.25, the surface progressively deprotonates and the density of ≡S–O^- groups grows, which makes the uptake more favorable. It must be stressed, however, that at the final pH of 5.5–6.3 measured in the experiments carried out at the natural pH, the solid is still below its point of zero charge and therefore carries a net positive charge, so that the lead retained under these conditions cannot be held by a global electrostatic attraction and must be bound by specific reactions with individual surface sites [25,27].

Care must be taken not to attribute to sorption what is in fact precipitation. The distribution of dissolved lead species computed with Visual MINTEQ, version 3.1 [58], for a total concentration of 100 mg L^{-1} at 25 °C is shown in Figure 6. The free Pb^{2+} ion dominates up to about pH 7.5; hydrolyzed cationic species—$PbOH^{+}$ from pH ≈ 5.5 and $Pb_3(OH)_4^{2+}$ from pH ≈ 7—appear and can also be retained by the sorbent, whereas the neutral $Pb(OH)_2$ complex, the precursor of the solid hydroxide, becomes significant only above pH 7.5. The value of 57.14 mg g^{-1} measured at pH_i ≈ 8 (and the values obtained at higher pH_i) must therefore be regarded with caution, since part of the removal may proceed through hydroxide precipitation. In contrast, all the experiments carried out at the natural pH ended at a final pH between 5.5 and 6.3, well inside the domain where Pb^{2+} is the dominant species, so that the precipitation of $Pb(OH)_2$ can safely be ruled out and the measured capacities can be ascribed to reactions with the solid (Section 4.6).

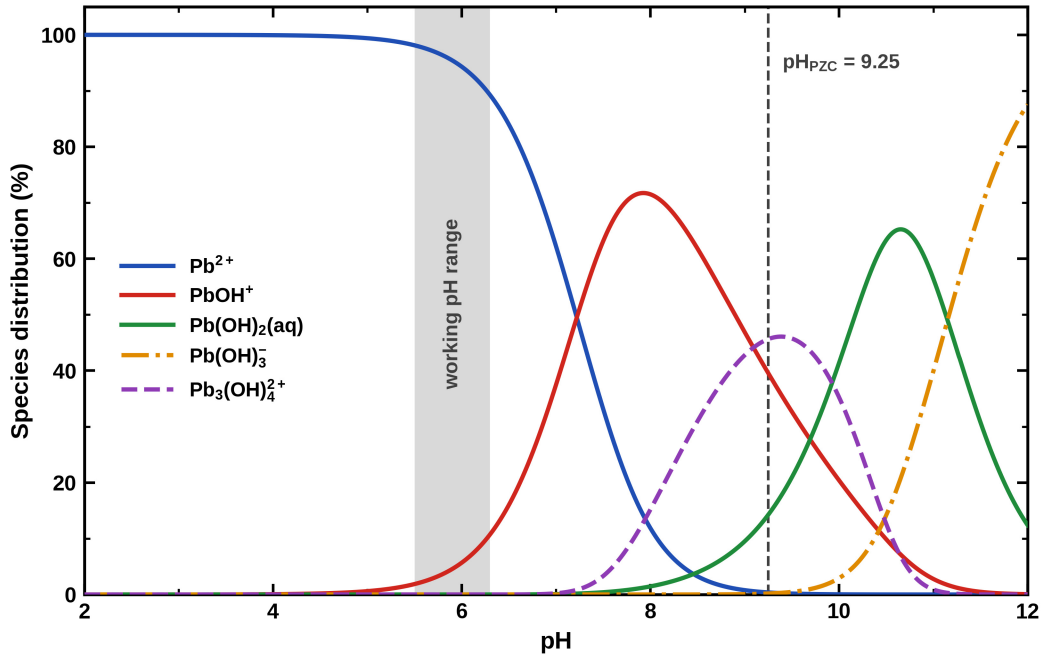


Figure 6. Distribution of dissolved Pb(II) species as a function of pH, computed for a total lead concentration of 100 mg L^{-1} at 25 °C. The shaded band indicates the range of final pH values measured in the experiments carried out at the natural pH (5.5–6.3); the dashed line marks the measured pH_{PZC}.

4.2. Rate-Controlling Step and Diffusion Mechanism

Equilibrium within 60 min places Mg_2Al–CO_3 among the faster LDH sorbents for lead: about 240 min was needed for alginate-intercalated MgAl–LDH [28] and 24 to 48 h for humate-modified Mg_3Al phases [25], although a CoMo–CO_3 phase reached equilibrium in 30 min [59]. The half-sorption time derived from the PFO constant is 8.3 min.

The clear superiority of the PFO equation over the PSO equation is the first indication that chemisorption is not the rate-controlling step, since the PSO model is usually associated with the formation of chemical bonds between the sorbate and the surface [50,56]. It should be stressed that this conclusion is only accessible through non-linear fitting: the linearized forms of both equations return comparably high correlation coefficients and would not discriminate between them [56].

The multilinearity of the $q_t = f(t_c^{1/2})$ plot identifies three successive transport regimes: external (film) diffusion up to about 40 min, intraparticle diffusion between 40 and 60 min, and the equilibrium plateau beyond. Because none of the segments passes through the origin, intraparticle diffusion is not the sole rate-limiting step [43,51]. The first segment

is markedly broader than the second, which indicates that external surface diffusion contributes substantially to the overall rate. This is consistent with the textural data: the porosity of the solid is mainly mesoporous, with a mean pore diameter of 6.6 nm, and the external surface accounts for 80.5% of S_{BET}, so that most of the accessible sites lie on the outer surface of the particles rather than inside a micropore network.

4.3. Nature of the Interaction

Three independent criteria show that the interaction is weak and does not involve the formation of strong covalent bonds over the whole of the retained lead, although, as shown below, it cannot be reduced to simple electrostatic attraction either. First, the enthalpy change, ΔH° = 11.07 kJ mol^{-1}, is of the order of 10 kJ mol^{-1}, a magnitude typical of electrostatic interactions rather than of true chemical bonding. The comparison with the literature is instructive here: Mostafa et al. reported 6.9 kJ mol^{-1} for Pb(II) on CoMo–CO_3 [59], whereas González et al. obtained more than 50 kJ mol^{-1} on humate-intercalated Mg_3Al and above 95 kJ mol^{-1} on Mg_3Al–Cl, values that point to chemisorption [25]. The nature of the interaction thus depends strongly on the LDH considered and, in particular, on the interlayer anion: a carbonate phase, in which the interlayer is occupied by a small, strongly held and non-chelating anion, is not expected to bind lead covalently.

Second, the mean free energy of sorption obtained from the D–R isotherm, 1.41 kJ mol^{-1}, is far below the 16 kJ mol^{-1} threshold above which chemisorption is considered to prevail. Third, the activation energy derived from the Arrhenius plot (Table S7), 1.96 kJ mol^{-1}, is an order of magnitude smaller than the 40 kJ mol^{-1} usually required for a chemically activated process [56]. The positive standard entropy change, ΔS° = 105.8 J mol^{-1} K^{-1} (Table 4), reflects the increase in randomness at the solid–solution interface that accompanies the release of hydration water when the metal ion binds to the surface, with the entropy gained by the released water molecules exceeding the entropy lost by the immobilized cation.

4.4. Effect of the Composition of the Hydroxide Layer

The results obtained here for Mg_2Al–CO_3 can be compared directly with those we published for Mg_2[FeAl]–CO_3 [42] and Zn_2[FeAl]–CO_3 [43], since the three solids were prepared, characterized and tested under strictly identical conditions (Section 2.6). Any difference in performance can therefore be attributed to the composition of the hydroxide layer rather than to the operating protocol. This is precisely what published data cannot provide: without a common protocol, the effect of the layer composition cannot be separated from that of the operating conditions (Section 1). Table 5 gathers the corresponding properties and capacities, and Figure 7 presents the resulting relationships; the effect of the trivalent cation is assessed by comparing Mg_2Al–CO_3 with Mg_2[FeAl]–CO_3 (Section 4.4.1), and that of the divalent cation by comparing Mg_2[FeAl]–CO_3 with Zn_2[FeAl]–CO_3 (Section 4.4.2).

Table 5. Comparison of Mg_2Al–CO_3 with the two isostructural phases previously studied under identical conditions.

Property	Mg_2Al–CO_3	Mg_2[FeAl]–CO_3	Zn_2[FeAl]–CO_3
Source	this work	[42]	[43]
Substitution	—(reference)	½ $Al^{III} \rightarrow Fe^{III}$ (vs. Mg_2Al–CO_3)	$Mg^{II} \rightarrow Zn^{II}$ (vs. Mg_2[FeAl]–CO_3)
a (Å)	3.0434	3.0746	3.0912
c (Å)	22.8402	22.9566	22.7460
d_{003} (Å)	7.61	7.65	7.58
Relative crystallinity (%)	67.96	46.92	59.60

Table 5. *Cont.*

Property	$Mg_2Al–CO_3$	$Mg_2[FeAl]–CO_3$	$Zn_2[FeAl]–CO_3$
M^{II}/M^{III} (EDX)	1.69	1.60	1.82
$x = M^{III}/(M^{II} + M^{III})$	0.372	0.385	0.354
S_{BET} ($m^2\ g^{-1}$)	37.83	80.77	54.48
External surface (%)	80.53	85.12	82.67
Mean pore diameter (nm)	6.62	5.03	5.13
Particle size (nm)	158.59	74.29	110.13
pH_{PZC}	9.25	9.35	8.35
q_e at C_0 = 100 mg L^{-1} (mg g^{-1})	27.11	36.46	31.23
q_e at C_0 = 300 mg L^{-1} (mg g^{-1})	46.31	78.54	65.06
$q_{m,L}$ (mg g^{-1})	59.06	118.78	87.89
Best isotherm	R–P ≈ Langmuir	R–P ≈ Langmuir	R–P ≈ Freundlich
$\Delta H°$ (kJ mol^{-1})	11.072	9.208	10.524

4.4.1. Partial Substitution of Al^{III} by Fe^{III}

Replacing half of the aluminum by iron, at constant divalent cation and constant nominal ratio, doubles the Langmuir capacity, from 59.06 to 118.78 mg g^{-1} [42], and raises the capacity measured at C_0 = 100 mg L^{-1} from 27.11 to 36.46 mg g^{-1}. The origin of this improvement appears to be textural rather than chemical. Fe^{III} has a larger ionic radius than Al^{III} (0.645 vs. 0.535 Å in octahedral coordination [60]), and its incorporation introduces local distortions in the hydroxide sheet that hinder the growth of large coherent domains. The lattice parameter a increases accordingly from 3.0434 to 3.0746 Å, the relative crystallinity falls from 68.0 to 46.9%, the equivalent particle size drops from 159 to 74 nm and the specific surface area more than doubles, from 37.8 to 80.8 $m^2\ g^{-1}$ [42] (Figure S9). The thermal data point in the same direction, the interlayer water being released 50 °C earlier in the iron-containing phase.

Because the surface chemistry is barely modified—pH_{PZC} moves only from 9.25 to 9.35, and the sorption enthalpy remains close to 10 kJ mol^{-1} in both cases—the gain in capacity is most reasonably ascribed to the increase in the number of accessible sites rather than to a change in their nature. Comparable observations have been reported for MgAl-LDHs prepared through different synthetic routes, where the least crystalline sample removed lead most efficiently [40]; a similar dependence on the synthesis route was reported for phosphate [41]. The same trend was observed for ternary Zn–Al–Fe phases, in which iron incorporation improved the sorption of oxyanions [61,62].

4.4.2. Replacement of Mg^{II} by Zn^{II}

The effect of the divalent cation is isolated by comparing $Mg_2[FeAl]–CO_3$ and $Zn_2[FeAl]–CO_3$, which have the same trivalent composition. Replacing Mg^{II} by Zn^{II} lowers the Langmuir capacity from 118.78 to 87.89 mg g^{-1} and q_e at C_0 = 100 mg L^{-1} from 36.46 to 31.23 mg g^{-1} [42,43]. This decrease again follows the texture: the zinc-based phase is more crystalline (59.6 vs. 46.9%) and exposes a smaller specific surface area (54.5 vs. 80.8 $m^2\ g^{-1}$). It occurs even though the point of zero charge drops by one unit, from 9.35 to 8.35, so that at the working pH of 5.5–6.3 the zinc-based surface carries a lower net positive charge, which should, if anything, favor the approach of Pb^{2+} [27]. The surface chemistry is nevertheless modified, as shown by the change in the shape of the isotherm: whereas $Mg_2Al–CO_3$ and $Mg_2[FeAl]–CO_3$ are both described by a Redlich–Peterson equation tending toward the Langmuir limit, $Zn_2[FeAl]–CO_3$ has an exponent β of 0.60 and is better represented by the Freundlich model, which points to a more heterogeneous distribution of site energies [43]. Compared with the binary $Mg_2Al–CO_3$ phase, $Zn_2[FeAl]–CO_3$ still retains more lead

(87.89 vs. 59.06 mg g^{-1}), but this difference combines the two substitutions and, here again, parallels the difference in specific surface area (54.5 vs. 37.8 m^2 g^{-1}).

Taken together, the two substitutions give the ranking Mg_2[FeAl]–CO_3 > Zn_2[FeAl]–CO_3 > Mg_2Al–CO_3 (Figure 7c), and the Langmuir capacity increases with the BET surface area and decreases with the relative crystallinity (Figure 7a,b). With only three materials, these correlations are indicative rather than demonstrative, and they should be extended to a larger series before being used predictively; nevertheless, they are consistent with the mechanistic picture developed in Section 4.6, in which the dominant pathways are surface reactions. Partial substitution of the trivalent cation appears to be the more effective lever of the two, since it increases the accessible surface without perturbing the surface chemistry, whereas replacing the divalent cation modifies texture and surface chemistry at the same time.

A further step can be taken. The capacities of the three phases differ by a factor of two, but they were obtained on solids whose specific surface areas also differ by a factor of two. Referred to the unit of accessible surface, the Langmuir capacities become 1.56, 1.47 and 1.61 mg m^{-2} for Mg_2Al–CO_3, Mg_2[FeAl]–CO_3 and Zn_2[FeAl]–CO_3 respectively, that is 1.55 ± 0.07 mg m^{-2}, a spread of only ±5% for compositions that differ in both the trivalent and the divalent position. Expressed as a surface density this corresponds to 4.5 ± 0.2 Pb nm^{-2}, a value of the same order as the density of hydroxyl groups exposed by a brucite-like sheet and close to one lead ion per two surface hydroxyls, that is to the stoichiometry of the bidentate complex discussed in Section 4.6. The intrinsic reactivity of the surface toward Pb(II) is therefore essentially invariant across the series: the composition of the hydroxide layer acts on the capacity through the amount of surface it generates, not through a change in the nature of the sites. The normalization is least reliable for Zn_2[FeAl]–CO_3, whose isotherm is better described by the Freundlich equation so that its Langmuir q_m is the least well defined of the three, and three solids are of course too few to establish a law; the invariance should be tested on a broader compositional series before being used predictively.

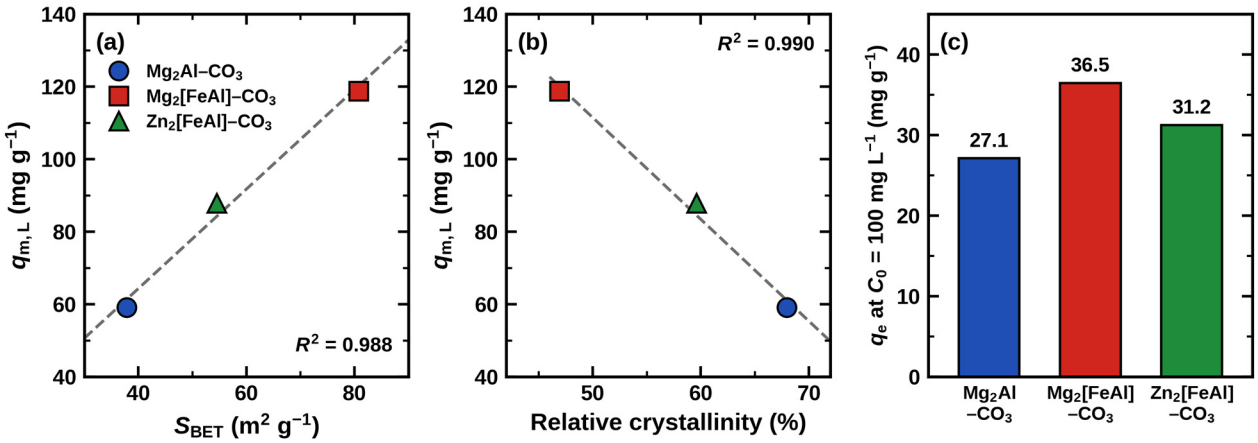


Figure 7. Relationships between Pb(II) sorption capacity and physicochemical properties for the three isostructural phases: (**a**) Langmuir capacity vs. BET surface area; (**b**) Langmuir capacity vs. relative crystallinity; (**c**) equilibrium capacity at C_0 = 100 mg L^{-1}. Data for Mg_2[FeAl]–CO_3 and Zn_2[FeAl]–CO_3 from [42] and [43], respectively.

4.5. Comparison with Other LDH Sorbents

Table 6 positions Mg_2Al–CO_3 among LDH sorbents reported for Pb(II), the entries being ordered by increasing maximum capacity. Because published maxima are not always obtained in the same way, the basis of each value is indicated: experimental maxima are

the highest capacities measured at the stated initial concentration, whereas Langmuir values are monolayer capacities extracted from a model fit and are usually higher than any capacity measured directly. The two categories should therefore not be compared too literally.

Several trends nevertheless emerge. The lower part of the table is occupied by phases intercalated with small organic ligands and tested at low initial concentration whose maxima remain below 40 mg g^{-1} [36,63]. The upper part is dominated by calcined or reconstructed phases and by materials intercalated with large chelating anions [25,28,37]. This is expected: calcination destroys the layered structure and generates a mixed oxide of much larger surface area that reconstructs in the presence of the sorbate, while chelating interlayer anions provide additional, strongly binding sites [64–66]. The price to pay is a more elaborate and more energy-intensive preparation, and often a much longer equilibration time—24 to 48 h for the humate-modified Mg_3Al phases against 60 min here.

Within the group of carbonate-intercalated LDHs used without any post-synthesis modification, $Mg_2Al–CO_3$ occupies an intermediate position, and its two substituted analogues rank among the better performers in Table 6 [42,43]. More elaborate architectures have also been developed recently, such as LDHs intercalated with $[Mo_2S_{12}]^{2-}$ or thiosulfate anions, LDH-based hydrogels and biochar or cellulose composites, and LDH-derived mixed oxides [67–72]; their preparation, however, is considerably more complex than that of the carbonate phases considered here. It is also worth noting that these three phases were tested without any pH adjustment, which removes a costly conditioning step in practical operation, and that they settle readily and are easily separated from the treated water.

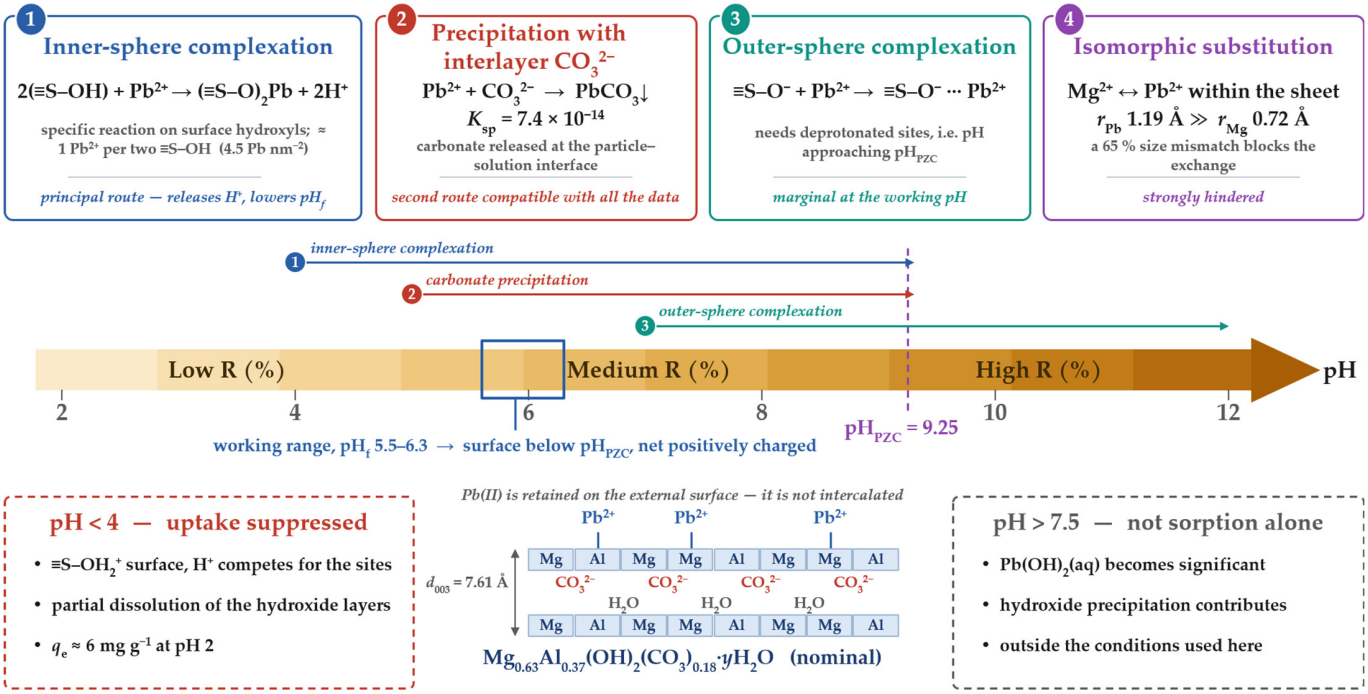
Table 6. Maximum Pb(II) sorption capacities reported for LDH sorbents, ordered by increasing Q_{max}.

Sorbent	C_0 (mg L^{-1})	m/V (g L^{-1})	t_c (h)	pH_i	Q_{max} (mg g^{-1})	Basis	Reference
Mg_2Al–glutamate	20	1	2	5	19.3	experimental	[36]
Mg_4Al–tartrate	100	1	2	5	20.5	experimental	[63]
Mg_2Al–Cl	200	1	2.5	5.5	37.0	experimental	[73]
Mg_3Al–humate (50%)	207.2	1.67	24	5	51.8	experimental	[25]
$Mg_2Al–CO_3$	300	1.75	3	unadjusted	59.1	Langmuir	this work
$CoMo–CO_3$	369.9	5	2	5.5	73.4	experimental	[59]
Zn_2[FeAl]–CO_3	300	1.75	3	unadjusted	87.9	Langmuir	[43]
Mg_3Al–humate (100%)	207.2	1.67	48	5	99.5	experimental	[25]
Mg_2[FeAl]–CO_3	300	1.75	3	unadjusted	118.8	Langmuir	[42]
Mg_3Al–Cl	207.2	1.67	24	5	126.4	experimental	[25]
MgAl–alginate	20.7–2486	2.5	4	5.5	243.7	Langmuir	[28]
MIL-88A(Fe)-derived LDH	85–280	0.4	24	3.0	512.8	Langmuir	[37]

"Experimental" denotes the highest capacity measured at the stated initial concentration; "Langmuir" denotes the monolayer capacity q_m obtained by fitting the Langmuir equation. For $Mg_2Al–CO_3$ the highest capacity measured directly was 46.3 mg g^{-1} at C_0 = 300 mg L^{-1}, and the value extrapolated from the $1/q_e = f(1/C_0)$ plot was 68.6 mg g^{-1}.

4.6. Proposed Removal Mechanism

The removal of metallic cations by LDHs is rarely governed by a single process [27,29,30]. The evidence collected here allows the relative importance of the different pathways to be assessed for $Mg_2Al–CO_3$ (Scheme 1).



Scheme 1. pH-dependent representation of the pathways proposed for Pb(II) removal by $Mg_2Al–CO_3$. The horizontal band follows the increase in removal efficiency with pH; cards 1–4 rank the pathways by their consistency with the measurements, and the colored spans give the pH domain over which each operates. At the working pH the surface lies below its point of zero charge and is net positively charged, so routes 1 and 2—not the electrostatic route 3—are the two pathways compatible with the whole of the data. The dashed boxes mark the two domains in which the measured uptake cannot be interpreted as sorption alone.

- Specific (inner-sphere) surface complexation. At the working pH of 5.5–6.3, the solid lies well below its point of zero charge (9.25) and its surface therefore carries a net positive charge, so that a simple electrostatic attraction of Pb^{2+} by deprotonated ≡S–O^- sites cannot be the dominant pathway. Uptake nevertheless occurs and rises steeply with pH, which points to a specific reaction with individual surface hydroxyls, a reaction that does not require the particle to be negatively charged as a whole: 2(≡S–OH) + Pb^{2+} → (≡S–O)$_2$Pb + 2H^+. This reaction releases protons, and it accounts for the slight but perfectly regular decrease of the final pH measured as the initial concentration increases, from 6.23 at 10 mg L^{-1} to 5.76 at 300 mg L^{-1}. It is further supported by the surface density of retained lead derived in Section 4.4, about 4.5 Pb nm^{-2}, which corresponds to roughly one lead ion per two surface hydroxyls of a brucite-like sheet, that is to the stoichiometry of the bidentate complex written above.
- Outer-sphere complexation. As the pH rises toward the point of zero charge the density of deprotonated ≡S–O^- groups grows and a non-specific, electrostatically driven contribution is added to the specific one. This second pathway accounts for the sharp rise of the capacity between pH_i 4 and 8 and is consistent with the low sorption enthalpy (11.07 kJ mol^{-1}) and the low mean free energy of sorption (1.41 kJ mol^{-1}), which exclude the formation of strong covalent bonds over the whole of the retained lead. At the unadjusted pH at which the present measurements were made, however, its contribution remains marginal.
- Surface precipitation with interlayer carbonate. Carbonate released at the particle–solution interface can precipitate lead as $PbCO_3$ (K_{sp} = 7.4 × 10^{-14}), a pathway documented for the reaction of $MgAl–CO_3$ with lead salts [27] and, more recently, for the mineralization of Pb(II) as hydrocerussite, $Pb_3(CO_3)_2(OH)_2$, by MgAl LDHs [74]. Precipitation as

$Pb(OH)_2$ is excluded here because the final pH of the experiments carried out at the natural pH never exceeded 6.3.

- Isomorphic substitution. Replacement of layer Mg^{2+} by Pb^{2+} is severely hindered by the size mismatch: the ionic radius of Pb^{2+} (1.19 Å) is 65% larger than that of Mg^{2+} (0.72 Å) [60]. This contrasts with Cu^{2+} (0.73 Å) and Cd^{2+} (0.95 Å), for which lattice substitution is a genuine pathway [25,75], and it explains why the capacities measured for Pb(II) on these carbonate phases are systematically lower, on a molar basis, than those measured for Cu(II) under identical conditions [43].

Since the two dominant pathways are surface reactions, the amount of accessible surface should control the capacity—which is precisely what the comparison in Section 4.4 shows. It also suggests that the relative weight of the pathways is composition-dependent: in Mg_2[FeAl]–CO_3 the larger external surface increases the contribution of the two complexation routes [42], whereas in Zn_2[FeAl]–CO_3 the more heterogeneous site distribution revealed by the Freundlich behavior suggests a greater diversity of binding environments [43]. This coupling between composition, microstructure and mechanism is, in our view, a major reason why capacities reported for nominally similar LDHs differ so widely.

5. Conclusions

A carbonate-intercalated Mg_2Al–CO_3 layered double hydroxide was prepared by coprecipitation at constant pH and evaluated for the removal of Pb(II) from aqueous solution. XRD confirmed a well-crystallized rhombohedral hydrotalcite-type phase with a basal spacing of 7.61 Å and a relative crystallinity of 68.0%, in close agreement with the reference card PDF-2 01-089-0460; SEM showed strongly agglomerated micrometric aggregates and EDX gave a surface Mg/Al ratio of 1.69, leading to the approximate composition $Mg_{0.63}Al_{0.37}(OH)_2(CO_3)_{0.18}\cdot yH_2O$; nitrogen sorption revealed a mesoporous solid with S_{BET} = 37.8 $m^2\ g^{-1}$, 80.5% of which is external; DSC resolved three endothermic events at 125, 225 and above 275 °C; and the point of zero charge was 9.25.

Sorption equilibrium was reached within 60 min, and the kinetics were well described by the pseudo-first-order equation, while the linearized intraparticle diffusion plot showed that external surface diffusion and pore diffusion operate in series. Equilibrium data were best represented by the Redlich–Peterson and Langmuir models, with a monolayer capacity of 59.1 mg g^{-1} and a favorable separation factor over the whole concentration range. The process is endothermic (ΔH° = 11.07 kJ mol^{-1}, a value independent of the standard state adopted) and spontaneous, ΔG°(298 K) being −20.5 kJ mol^{-1} when referred to C° = 1 mol L^{-1}, with ΔS° = 106 J mol^{-1} K^{-1}. Since all the experiments carried out at the natural pH ended at a final pH well below the point of zero charge, the removal cannot be ascribed to a simple electrostatic attraction: specific complexation on surface hydroxyls, with release of protons, and surface precipitation with the interlayer carbonate are the two pathways compatible with the whole of the data.

Comparison with two isostructural phases studied earlier under strictly identical conditions gives the practical message of this work. Partial substitution of Al^{III} by Fe^{III} doubles the monolayer capacity, from 59.1 to 118.8 mg g^{-1} [42], whereas the subsequent replacement of Mg^{II} by Zn^{II} lowers it to 87.9 mg g^{-1} [43]. In both cases the capacity follows the specific surface area and varies inversely with the crystallinity, and the trivalent substitution is the more effective lever because it acts on the texture without altering the surface chemistry. Designing an LDH sorbent for divalent metals should therefore aim at maximizing accessible surface area rather than structural perfection.

These conclusions rest on three materials and should be verified in a broader compositional series before being generalized. Further work should also extend the comparison to real effluents containing competing cations, examine the regeneration and reuse of the

iron-substituted phase, and test whether the crystallinity–capacity relationship still holds after calcination and reconstruction.

Supplementary Materials: The following supporting information can be downloaded at https://www.mdpi.com/article/10.3390/separations13100284/s1: Table S1. Interplanar distances and relative intensities of the main X-ray reflections of the synthesized Mg_2Al–CO_3 compared with those of the most compatible reference phase, $Mg_{0.667}Al_{0.333}(OH)_2(CO_3)_{0.167}{\cdot}0.5H_2O$ (PDF-2 01-089-0460, figure of merit 0.892). Figure S1. Scanning electron micrographs of Mg_2Al–CO_3 recorded at (a) 1.00 kx, (b) 2.00 kx and (c) 5.00 kx; secondary-electron mode, 25 kV. Figure S2. EDX spectrum of Mg_2Al–CO_3 recorded at 25 kV; the inset shows the analyzed area. Table S2. Surface chemical composition of Mg_2Al–CO_3 determined by EDX. Table S3. Detailed textural properties of Mg_2Al–CO_3 obtained from the nitrogen adsorption–desorption isotherms recorded at 77 K. Figure S3. DSC curve of Mg_2Al–CO_3 recorded between 40 and 500 °C at 10 °C min^{-1} under a nitrogen flow of 50 mL min^{-1}. The three endothermic domains (i), (ii) and (iii) are discussed in the text. Figure S4. Determination of the point of zero charge of Mg_2Al–CO_3 by the batch equilibration method (NaCl 0.01 M, 50 mL, 0.15 g of solid, 48 h, room temperature). The intersection of $pH_f = f(pH_i)$ with the first bisector gives pH_{PZC} = 9.25. Table S4. Effect of the m/V ratio on the removal of Pb(II) by Mg_2Al–CO_3 (C_0 = 100 mg L^{-1}, V = 20 mL, pH_i = 5.45, t_c = 3 h, T = 25 °C). Figure S5. Effect of the initial pH on the sorption of Pb(II) by Mg_2Al–CO_3: (a) equilibrium capacity and removal efficiency; (b) final pH, as a function of the initial pH (C_0 = 100 mg L^{-1}, V = 20 mL, m/V = 1.75 g L^{-1}, t_c = 3 h, T = 25 °C; pH_i adjusted with 1 M HCl or 1 M NaOH). The shaded area marks the experiments that ended at $pH_f > 7.5$, for which precipitation of $Pb(OH)_2$ may contribute to the removal. Figure S6. Linearized intraparticle diffusion plot for the sorption of Pb(II) on Mg_2Al–CO_3. Three linear segments are resolved: external surface diffusion (I, $t_c < 40$ min), intraparticle diffusion (II, 40–60 min) and the equilibrium plateau (III, $t_c > 60$ min). Table S5. Parameters of the linearized intraparticle diffusion model for the sorption of Pb(II) on Mg_2Al–CO_3. Figure S7. Effect of the initial Pb(II) concentration on the equilibrium capacity of Mg_2Al–CO_3 (m/V = 1.75 g L^{-1}, t_c = 3 h, T = 25 °C). Table S6. Effect of the initial Pb(II) concentration on the equilibrium capacity and on the final pH for Mg_2Al–CO_3 (m/V = 1.75 g L^{-1}, t_c = 3 h, T = 25 °C). Table S7. Non-linear pseudo-first-order parameters for the sorption of Pb(II) on Mg_2Al–CO_3 as a function of temperature. Figure S8. Comparison of the BET specific surface area and of the relative crystallinity of the three isostructural carbonate phases. Data for Mg_2[FeAl]–CO_3 and Zn_2[FeAl]–CO_3 are taken from Ait Ichou et al. (2020) [42] and Ait Ichou et al. (2023) [43], respectively, as cited in the main text. Table S8. Data for Figure 2a: effect of the sorbent dose on the removal efficiency of Pb(II) by Mg_2Al–CO_3 (C_0 = 100 mg L^{-1}, V = 20 mL, pH_i = 5.45, t_c = 3 h, T = 25 °C). Table S9. Data for Figure 2b: effect of the sorbent dose on the equilibrium capacity of Mg_2Al–CO_3 toward Pb(II) (C_0 = 100 mg L^{-1}, V = 20 mL, pH_i = 5.45, t_c = 3 h, T = 25 °C). Table S10. Data for Figure 3 and Figure S6: sorption kinetics of Pb(II) on Mg_2Al–CO_3 (C_0 = 100 mg L^{-1}, m/V = 1.75 g L^{-1}, pH_i = 5.45, T = 25 °C). Table S11. Data for Figure 4 and Figure S7: effect of the initial Pb(II) concentration on the equilibrium capacity of Mg_2Al–CO_3 (m/V = 1.75 g L^{-1}, t_c = 3 h, T = 25 °C). The corresponding mean equilibrium concentrations C_e are given in Table S6. Table S12. Data for Figure 5a: effect of temperature on the equilibrium capacity of Mg_2Al–CO_3 toward Pb(II) (C_0 = 100 mg L^{-1}, m/V = 1.75 g L^{-1}, t_c = 3 h, pH_i = 5.45). Table S13. Data for Figure S5a: effect of the initial pH on the equilibrium capacity of Mg_2Al–CO_3 toward Pb(II) (C_0 = 100 mg L^{-1}, V = 20 mL, m/V = 1.75 g L^{-1}, t_c = 3 h, T = 25 °C). Table S14. Data for Figure S5a: effect of the initial pH on the removal efficiency of Pb(II) by Mg_2Al–CO_3 (C_0 = 100 mg L^{-1}, V = 20 mL, m/V = 1.75 g L^{-1}, t_c = 3 h, T = 25 °C). Table S15. Data for Figure S5b: final pH as a function of the initial pH (C_0 = 100 mg L^{-1}, V = 20 mL, m/V = 1.75 g L^{-1}, t_c = 3 h, T = 25 °C).

Author Contributions: Conceptualization, A.A.I. and F.S.; methodology, A.A.I., R.B. and M.A.; software, A.A.I.; validation, G.C., M.C. and M.Z.; formal analysis, A.A.I. and A.D.; investigation, A.A.I., R.B. and A.D.; resources, G.C. and F.S.; data curation, A.A.I. and A.S.; writing—original draft preparation, A.A.I.; writing—review and editing, F.S., M.C., M.Z., G.C. and A.S.; visualization, A.A.I.

and M.A.; supervision, F.S. and M.Z.; project administration, F.S.; funding acquisition, F.S. All authors have read and agreed to the published version of the manuscript.

Funding: This research received no external funding.

Data Availability Statement: The data presented in this study are available on request from the corresponding author. Data for Mg_2[FeAl]–CO_3 and Zn_2[FeAl]–CO_3 are those published in refs. [42,43].

Conflicts of Interest: The authors declare no conflicts of interest.

Abbreviations

The following abbreviations are used in this manuscript:

LDH	Layered double hydroxide
XRD	X-ray diffraction
SEM–EDX	Scanning electron microscopy with energy-dispersive X-ray spectroscopy
BET	Brunauer–Emmett–Teller
BJH	Barrett–Joyner–Halenda
DSC	Differential scanning calorimetry
pH_{PZC}	pH of the point of zero charge
PFO/PSO	Pseudo-first-order/pseudo-second-order
IPD	Intraparticle diffusion
R–P	Redlich–Peterson
D–R	Dubinin–Radushkevich

References

1. Chen, J.P. *Decontamination of Heavy Metals: Processes, Mechanisms, and Applications*; CRC Press: Boca Raton, FL, USA, 2012.
2. Chaoua, S.; Boussaa, S.; El Gharmali, A.; Boumezzough, A. Impact of Irrigation with Wastewater on Accumulation of Heavy Metals in Soil and Crops in the Region of Marrakech in Morocco. *J. Saudi Soc. Agric. Sci.* **2019**, *18*, 429–436. [CrossRef]
3. Hashim, M.A.; Mukhopadhyay, S.; Sahu, J.N.; Sengupta, B. Remediation Technologies for Heavy Metal Contaminated Groundwater. *J. Environ. Manag.* **2011**, *92*, 2355–2388. [CrossRef] [PubMed]
4. World Health Organization. *Guidelines for Drinking-Water Quality: Fourth Edition Incorporating the First, Second and Third Addenda*; World Health Organization: Geneva, Switzerland, 2026; ISBN 978-92-4-012122-5.
5. Bashir, A.; Malik, L.A.; Ahad, S.; Manzoor, T.; Bhat, M.A.; Dar, G.N.; Pandith, A.H. Removal of Heavy Metal Ions from Aqueous System by Ion-Exchange and Biosorption Methods. *Environ. Chem. Lett.* **2019**, *17*, 729–754. [CrossRef]
6. Zawierucha, I.; Kozlowski, C.; Malina, G. Immobilized Materials for Removal of Toxic Metal Ions from Surface/Groundwaters and Aqueous Waste Streams. *Environ. Sci. Process. Impacts* **2016**, *18*, 429–444. [CrossRef] [PubMed]
7. Chiban, M.; Soudani, A.; Sinan, F.; Persin, M. Single, Binary and Multi-Component Adsorption of Some Anions and Heavy Metals on Environmentally Friendly *Carpobrotus edulis* Plant. *Colloids Surf. B* **2011**, *82*, 267–276. [CrossRef] [PubMed]
8. Kovacova, Z.; Demcak, S.; Balintova, M.; Pla, C.; Zinicovscaia, I. Influence of Wooden Sawdust Treatments on Cu(II) and Zn(II) Removal from Water. *Materials* **2020**, *13*, 3575. [CrossRef] [PubMed]
9. Ahmad, S.; Wazir, M.B.; Daud, M.; Cheng, C.K.; Shah, M.U.H.; Al-Harthi, M.A. Recent Advancement in Ionic Liquid Modified Layered Double Hydroxide (IL-LDH): Progress, Challenges, and Future Prospects. *Inorg. Chem. Commun.* **2023**, *158*, 111591. [CrossRef]
10. Al-Amrani, W.A.; Onaizi, S.A. Adsorptive Removal of Heavy Metals from Wastewater Using Emerging Nanostructured Materials: A State-of-the-Art Review. *Sep. Purif. Technol.* **2024**, *343*, 127018. [CrossRef]
11. Ismail, U.M.; Vohra, M.S.; Onaizi, S.A. Adsorptive Removal of Heavy Metals from Aqueous Solutions: Progress of Adsorbents Development and Their Effectiveness. *Environ. Res.* **2024**, *251*, 118562. [CrossRef] [PubMed]
12. Cavani, F.; Trifirò, F.; Vaccari, A. Hydrotalcite-Type Anionic Clays: Preparation, Properties and Applications. *Catal. Today* **1991**, *11*, 173–301. [CrossRef]
13. Evans, D.G.; Slade, R.C.T. Structural Aspects of Layered Double Hydroxides. In *Structure and Bonding*; Springer: Berlin/Heidelberg, Germany, 2006; pp. 1–87.
14. Forano, C.; Costantino, U.; Prevot, V.; Taviot-Gueho, C. Layered Double Hydroxides (LDH). In *Developments in Clay Science*; Elsevier: Amsterdam, The Netherlands, 2013; pp. 745–782.
15. Goh, K.-H.; Lim, T.-T.; Dong, Z. Application of Layered Double Hydroxides for Removal of Oxyanions: A Review. *Water Res.* **2008**, *42*, 1343–1368. [CrossRef] [PubMed]

16. Ulibarri, M.A.; Hermosin, M.C. Layered Double Hydroxides in Water Decontamination. In *Layered Double Hydroxides: Present and Future*; Nova Science Publishers: New York, NY, USA, 2006; pp. 285–321.
17. Kameliya, J.; Verma, A.; Dutta, P.; Arora, C.; Vyas, S.; Varma, R.S. Layered Double Hydroxide Materials: A Review on Their Preparation, Characterization, and Applications. *Inorganics* **2023**, *11*, 121. [CrossRef]
18. Fu, Y.; Fu, X.; Song, W.; Li, Y.; Li, X.; Yan, L. Recent Progress of Layered Double Hydroxide-Based Materials in Wastewater Treatment. *Materials* **2023**, *16*, 5723. [CrossRef] [PubMed]
19. Riaz, S.; ur Rehman, A.; Akhter, Z.; Najam, T.; Hossain, I.; Karim, M.R.; Assiri, M.A.; Shah, S.S.A.; Nazir, M.A. Recent Advancement in Synthesis and Applications of Layered Double Hydroxides (LDHs) Composites. *Mater. Today Sustain.* **2024**, *27*, 100897. [CrossRef]
20. Altalhi, A.A.; Mohamed, E.A.; Negm, N.A. Recent Advances in Layered Double Hydroxide (LDH)-Based Materials: Fabrication, Modification Strategies, Characterization, Promising Environmental Catalytic Applications, and Prospective Aspects. *Energy Adv.* **2024**, *3*, 2136–2151. [CrossRef]
21. Johnston, A.L.; Lester, E.; Williams, O.; Gomes, R.L. Understanding Layered Double Hydroxide Properties as Sorbent Materials for Removing Organic Pollutants from Environmental Waters. *J. Environ. Chem. Eng.* **2021**, *9*, 105197. [CrossRef]
22. Alagha, O.; Manzar, M.S.; Zubair, M.; Anil, I.; Mu'azu, N.D.; Qureshi, A. Magnetic Mg-Fe/LDH Intercalated Activated Carbon Composites for Nitrate and Phosphate Removal from Wastewater: Insight into Behavior and Mechanisms. *Nanomaterials* **2020**, *10*, 1361. [CrossRef] [PubMed]
23. Flores, C.V.; Obeso, J.L.; Herrera-Zuñiga, L.; Peralta, R.A.; Campero-Domínguez, J.I.; Morales-Ruiz, L.; Portillo-Vélez, N.S.; Valdivia-Corona, J.C. Layered Double Hydroxides (LDH) Materials for Effective Phosphate Adsorption from Aqueous Solution. *RSC Sustain.* **2026**, *4*, 61–78. [CrossRef]
24. Farhan, A.; Khalid, A.; Maqsood, N.; Iftekhar, S.; Sharif, H.M.A.; Qi, F.; Sillanpaa, M.; Asif, M.B. Progress in Layered Double Hydroxides (LDHs): Synthesis and Application in Adsorption, Catalysis and Photoreduction. *Sci. Total Environ.* **2024**, *912*, 169160. [CrossRef] [PubMed]
25. González, M.A.; Pavlovic, I.; Barriga, C. Cu(II), Pb(II) and Cd(II) Sorption on Different Layered Double Hydroxides. A Kinetic and Thermodynamic Study and Competing Factors. *Chem. Eng. J.* **2015**, *269*, 221–228. [CrossRef]
26. Shan, R.; Yan, L.; Yang, K.; Hao, Y.; Du, B. Adsorption of Cd(II) by Mg–Al–CO3– and Magnetic Fe3O4/Mg–Al–CO3-Layered Double Hydroxides: Kinetic, Isothermal, Thermodynamic and Mechanistic Studies. *J. Hazard. Mater.* **2015**, *299*, 42–49. [CrossRef] [PubMed]
27. Liang, X.; Zang, Y.; Xu, Y.; Tan, X.; Hou, W.; Wang, L.; Sun, Y. Sorption of Metal Cations on Layered Double Hydroxides. *Colloids Surf. A* **2013**, *433*, 122–131. [CrossRef]
28. Zhang, X.; Shan, R.; Li, X.; Yan, L.; Ma, Z.; Jia, R.; Sun, S. Effective Removal of Cu(II), Pb(II) and Cd(II) by Sodium Alginate Intercalated MgAl-Layered Double Hydroxide: Adsorption Properties and Mechanistic Studies. *Water Sci. Technol.* **2021**, *83*, 975–984. [CrossRef] [PubMed]
29. Feng, X.; Long, R.; Wang, L.; Liu, C.; Bai, Z.; Liu, X. A Review on Heavy Metal Ions Adsorption from Water by Layered Double Hydroxide and Its Composites. *Sep. Purif. Technol.* **2022**, *284*, 120099. [CrossRef]
30. Ahmed, M.A.; Mohamed, A.A. A Systematic Review of Layered Double Hydroxide-Based Materials for Environmental Remediation of Heavy Metals and Dye Pollutants. *Inorg. Chem. Commun.* **2023**, *148*, 110325. [CrossRef]
31. Brahma, D.; Barman, M.P.; Basak, D.; Saikia, H. Prospects of Layered Double Hydroxide (LDH)-Based Adsorbents for the Remediation of Environmental Inorganic Pollutants from Wastewater: A Critical Review. *Environ. Sci. Water Res. Technol.* **2025**, *11*, 830–875. [CrossRef]
32. Rana, I.; Prajapat, A.; Singh, M.B.; Hitesh; Ebenso, E.E.; Verma, C.; Msagati, T.A.M.; Pandey, G.; Patel, R.; AlFantazi, A.; et al. A Comprehensive Review of Heavy Metal Ions Removal Using 2-D Materials: Mechanism, Surface Chemistry, and Coordination Bonding. *Coord. Chem. Rev.* **2026**, *558*, 217774. [CrossRef]
33. Dai, C.; Wu, X.; Wang, Q.; Bai, Y.; Zhao, D.; Fu, J.; Fu, B.; Ding, H. Layered Double Hydroxides for Efficient Treatment of Heavy Metals and Organic Pollutants: Recent Progress and Future Perspectives. *Sep. Purif. Technol.* **2025**, *352*, 128277. [CrossRef]
34. Deng, H.; Zhang, S.; Li, Q.; Li, A.; Gan, W.; Hu, L. Efficient Removal of Lead, Cadmium, and Zinc from Water and Soil by MgFe Layered Double Hydroxide: Adsorption Properties and Mechanisms. *Sustainability* **2024**, *16*, 11037. [CrossRef]
35. Shafiq, M.; Alazba, A.A.; Amin, M.T. Preparation of ZnMgAl-Layered Double Hydroxide and Rice Husk Biochar Composites for Cu(II) and Pb(II) Ions Removal from Synthetic Wastewater. *Water* **2023**, *15*, 2207. [CrossRef]
36. Shen, Y.; Liu, D.; Li, S.; Fan, L.; Chen, S.; Haque, M.A. Removal of Lead from Aqueous Solution on Glutamate Intercalated Layered Double Hydroxide. *Arab. J. Chem.* **2017**, *10*, S2295–S2301. [CrossRef]
37. Huo, J.-B.; Yu, G. Layered Double Hydroxides Derived from MIL-88A(Fe) as an Efficient Adsorbent for Enhanced Removal of Lead(II) from Water. *Int. J. Mol. Sci.* **2022**, *23*, 14556. [CrossRef] [PubMed]
38. Hadnadjev-Kostic, M.; Vulic, T.; Karanovic, D.; Tomic, A.; Cvetkovic, D. Layered Double Hydroxide-Based Materials for Wastewater Treatment: Recent Progress in Multifunctional Environmental Applications. *Processes* **2025**, *13*, 3757. [CrossRef]

39. Huo, J.; Min, X.; Dong, Q.; Xu, S.; Wang, Y. Comparison of Zn–Al and Mg–Al Layered Double Hydroxides for Adsorption of Perfluorooctanoic Acid. *Chemosphere* **2022**, *287*, 132297. [CrossRef] [PubMed]
40. Mureseanu, M.; Eliescu, A.; Ignat, E.-C.; Carja, G.; Cioatera, N. Different Routes of MgAl–LDH Synthesis for Tailoring the Adsorption of Pb(II) Pollutant from Water. *C. R. Chim.* **2022**, *25*, 1–12. [CrossRef]
41. Benhiti, R.; Ait Ichou, A.; Zaghloul, A.; Aziam, R.; Carja, G.; Zerbet, M.; Sinan, F.; Chiban, M. Synthesis, Characterization, and Comparative Study of MgAl-LDHs Prepared by Standard Coprecipitation and Urea Hydrolysis Methods for Phosphate Removal. *Environ. Sci. Pollut. Res.* **2020**, *27*, 45767–45774. [CrossRef] [PubMed]
42. Ait Ichou, A.; Benhiti, R.; Abali, M.; Dabagh, A.; Chiban, M.; Zerbet, M.; Carja, G.; Sinan, F. Adsorption of Pb(II) from Aqueous Solutions onto MgFeAl-CO3 LDH: Thermodynamic and Kinetic Studies. *Desalin. Water Treat.* **2020**, *178*, 193–202. [CrossRef]
43. Ait Ichou, A.; Benhiti, R.; Abali, M.; Dabagh, A.; Carja, G.; Soudani, A.; Chiban, M.; Zerbet, M.; Sinan, F. Characterization and Sorption Study of Zn2[FeAl]-CO3 Layered Double Hydroxide for Cu(II) and Pb(II) Removal. *J. Solid State Chem.* **2023**, *320*, 123869. [CrossRef]
44. Brunauer, S.; Emmett, P.H.; Teller, E. Adsorption of Gases in Multimolecular Layers. *J. Am. Chem. Soc.* **1938**, *60*, 309–319. [CrossRef]
45. Barrett, E.P.; Joyner, L.G.; Halenda, P.P. The Determination of Pore Volume and Area Distributions in Porous Substances. I. Computations from Nitrogen Isotherms. *J. Am. Chem. Soc.* **1951**, *73*, 373–380. [CrossRef]
46. Thommes, M.; Kaneko, K.; Neimark, A.V.; Olivier, J.P.; Rodriguez-Reinoso, F.; Rouquerol, J.; Sing, K.S.W. Physisorption of Gases, with Special Reference to the Evaluation of Surface Area and Pore Size Distribution (IUPAC Technical Report). *Pure Appl. Chem.* **2015**, *87*, 1051–1069. [CrossRef]
47. Crini, G.; Badot, P.-M. *Traitement et Epuration des Eaux Industrielles Polluees*; Presses Universitaires de Franche-Comte: Besancon, France, 2007.
48. Abidar, F.; Morghi, M.; Ait Ichou, A.; Soudani, A.; Chiban, M.; Sinan, F.; Zerbet, M. Removal of Orthophosphate Ions from Aqueous Solution Using Chitin as Natural Adsorbent. *Desalin. Water Treat.* **2016**, *57*, 14739–14749. [CrossRef]
49. Lagergren, S. Zur Theorie Der Sogenannten Adsorption Gelöster Stoffe. *K. Sven. Vetenskapsakad. Handl.* **1898**, *24*, 1–39.
50. Ho, Y.S.; McKay, G. Pseudo-Second Order Model for Sorption Processes. *Process Biochem.* **1999**, *34*, 451–465. [CrossRef]
51. Weber, W.J.; Morris, J.C. Kinetics of Adsorption on Carbon from Solution. *J. Sanit. Eng. Div.* **1963**, *89*, 31–60. [CrossRef]
52. Langmuir, I. The Adsorption of Gases on Plane Surfaces of Glass, Mica and Platinum. *J. Am. Chem. Soc.* **1918**, *40*, 1361–1403. [CrossRef]
53. Freundlich, H.M.F. Over the Adsorption in Solution. *J. Phys. Chem.* **1906**, *57*, 385–470. [CrossRef]
54. Redlich, O.; Peterson, D.L. A Useful Adsorption Isotherm. *J. Phys. Chem.* **1959**, *63*, 1024. [CrossRef]
55. Temkin, M.I.; Pyzhev, V. Kinetics of Ammonia Synthesis on Promoted Iron Catalysts. *Acta Physicochim. URSS* **1940**, *12*, 217–222.
56. Tran, H.N.; You, S.-J.; Hosseini-Bandegharaei, A.; Chao, H.-P. Mistakes and Inconsistencies Regarding Adsorption of Contaminants from Aqueous Solutions: A Critical Review. *Water Res.* **2017**, *120*, 88–116. [CrossRef] [PubMed]
57. Dubinin, M.M.; Radushkevich, L.V. Equation of the Characteristic Curve of Activated Charcoal. *Proc. Acad. Sci. USSR Phys. Chem. Sect.* **1947**, *55*, 331–333.
58. Gustafsson, J.P. Visual MINTEQ. 2020. Available online: https://vminteq.com/ (accessed on 1 September 2026).
59. Mostafa, M.S.; Bakr, A.-S.A.; El Naggar, A.M.A.; Sultan, E.-S.A. Water Decontamination via the Removal of Pb(II) Using a New Generation of Highly Energetic Surface Nano-Material: $Co^{+2}Mo^{+6}$ LDH. *J. Colloid Interface Sci.* **2016**, *461*, 261–272. [CrossRef] [PubMed]
60. Shannon, R.D. Revised Effective Ionic Radii and Systematic Studies of Interatomic Distances in Halides and Chalcogenides. *Acta Crystallogr. Sect. A* **1976**, *32*, 751–767. [CrossRef]
61. Rezak, N.; Bahmani, A.; Bettahar, N. Adsorptive Removal of P(V) and Cr(VI) by Calcined Zn-Al-Fe Ternary LDHs. *Water Sci. Technol.* **2021**, *83*, 2504–2517. [CrossRef] [PubMed]
62. Carja, G.; Ratoi, S.; Ciobanu, G.; Balasanian, I. Uptake of As(V) from Aqueous Solution by Anionic Clays Type FeLDHs. *Desalination* **2008**, *223*, 243–248. [CrossRef]
63. Yasin, Y.; Mohamad, M.; Saad, A.; Sanusi, A.; Ahmad, F.H. Removal of Lead Ions from Aqueous Solutions Using Intercalated Tartrate-Mg–Al Layered Double Hydroxides. *Desalin. Water Treat.* **2014**, *52*, 4266–4272. [CrossRef]
64. Pérez, M.R.; Pavlovic, I.; Barriga, C.; Cornejo, J.; Hermosín, M.C.; Ulibarri, M.A. Uptake of Cu2+, Cd2+ and Pb2+ on Zn–Al Layered Double Hydroxide Intercalated with EDTA. *Appl. Clay Sci.* **2006**, *32*, 245–251. [CrossRef]
65. Rojas, R.; Perez, M.R.; Erro, E.M.; Ortiz, P.I.; Ulibarri, M.A.; Giacomelli, C.E. EDTA Modified LDHs as Cu2+ Scavengers: Removal Kinetics and Sorbent Stability. *J. Colloid Interface Sci.* **2009**, *331*, 425–431. [CrossRef] [PubMed]
66. Kameda, T.; Saito, S.; Umetsu, Y. Mg–Al Layered Double Hydroxide Intercalated with Ethylenediaminetetraacetate Anion: Synthesis and Application to the Uptake of Heavy Metal Ions from an Aqueous Solution. *Sep. Purif. Technol.* **2005**, *47*, 20–26. [CrossRef]

67. Roy, S.C.; Donley, C.L.; Islam, S.M. Efficient Sequestration of Heavy Metal Cations by $[Mo_2S_{12}]^{2-}$ Intercalated Cobalt Aluminum-Layered Double Hydroxide. *Inorganics* **2025**, *13*, 50. [CrossRef]
68. Li, J.; Wei, Y.; Zou, L.; Luo, Y.; Liu, Y.; Li, S. Study on the Adsorption Mechanism of Heavy Metal Ions by Thiosulfate-Intercalated ZnAl-LDH. *Inorg. Chem. Commun.* **2025**, *179*, 114771. [CrossRef]
69. Elamin, N.Y.; Mubarak, M.F.; Elamin, M.R.; Altalhi, A.A.; Bendary, H.I.; Mohamed, E.A. Synergistic Alginate/MgAl-LDH/Polypyrrole Interpenetrating Network Hydrogel for Selective Pb(II) and Rhodamine B Removal: Mechanistic, Kinetic and Thermodynamic Evaluation. *Surf. Interfaces* **2026**, *87*, 109021. [CrossRef]
70. Akhtar, R.; Khan, A.; Gul, M.; Anjum, M.A.R.; Rafique, I.; Rehan, M.; Qureshi, R.N.; Iqbal, S.; Saifullah, M. Facile Synthesis of Cobalt-Iron Layered Double Hydroxide and Its Derived Mixed Metal Oxide for Congo Red and Pb(II) Remediation. *Colloids Surf. C Environ. Asp.* **2026**, *4*, 100095. [CrossRef]
71. Huang, Y.; Liu, C.; Qin, L.; Xie, M.; Xu, Z.; Yu, Y. Efficient Adsorption Capacity of MgFe-Layered Double Hydroxide Loaded on Pomelo Peel Biochar for Cd(II) from Aqueous Solutions: Adsorption Behaviour and Mechanism. *Molecules* **2023**, *28*, 4538. [CrossRef] [PubMed]
72. El Messaoudi, N.; Miyah, Y.; Georgin, J.; Franco, D.S.P.; Sewwandi, B.V.N.; Singh, N.; Knani, S. A Review of LDH-Cellulose Hybrid Adsorbents for Organic and Inorganic Pollutant Removal from Wastewater. *Int. J. Biol. Macromol.* **2025**, *330*, 147986. [CrossRef] [PubMed]
73. Liang, X.; Hou, W.; Xu, Y.; Sun, G.; Wang, L.; Sun, Y.; Qin, X. Sorption of Lead Ion by Layered Double Hydroxide Intercalated with Diethylenetriaminepentaacetic Acid. *Colloids Surf. A Physicochem. Eng. Asp.* **2010**, *366*, 50–57. [CrossRef]
74. Wang, H.; Lin, T.; Song, Z.; Huang, M.; Chai, R.; An, S.; Song, Y.-F. Simultaneous Mineralization of Cd(II), Pb(II) and As(V) Using MgAl-NO_3: Performance and Mechanism. *Sep. Purif. Technol.* **2025**, *362*, 131853. [CrossRef]
75. Richardson, M.C.; Braterman, P.S. Cation Exchange by Anion-Exchanging Clays: The Effects of Particle Aging. *J. Mater. Chem.* **2009**, *19*, 7965–7975. [CrossRef]

Disclaimer/Publisher's Note: The statements, opinions and data contained in all publications are solely those of the individual author(s) and contributor(s) and not of MDPI and/or the editor(s). MDPI and/or the editor(s) disclaim responsibility for any injury to people or property resulting from any ideas, methods, instructions or products referred to in the content.